Verheye *et al.*
Journal of Hematology & Oncology (2024) 17:107
https://doi.org/10.1186/s13045-024-01629-3

Journal of Hematology & Oncology

RESEARCH

Open Access

A single-cell transcriptomic map of the murine and human multiple myeloma immune microenvironment across disease stages

Emma Verheye[1,2,3], Daliya Kancheva[1,3], Hatice Satilmis[2], Niels Vandewalle[2], Rong Fan[2], Pauline M. R. Bardet[1,3], Emile J. Clappaert[1,3], Kevin Verstaen[4,5], Ann De Becker[6], Karin Vanderkerken[2], Kim De Veirman[2,6*†] and Damya Laoui[1,3*†]

Abstract

Background The long-term effectiveness of immunotherapies against Multiple Myeloma (MM) remains elusive, demonstrated by the inevitable relapse in patients. This underscores the urgent need for an in-depth analysis of the MM tumor-immune microenvironment (TME). Hereto, a representative immunocompetent MM mouse model can offer a valuable approach to study the dynamic changes within the MM-TME and to uncover potential resistance mechanisms hampering effective and durable therapeutic strategies in MM.

Methods We generated a comprehensive single-cell RNA-sequencing atlas of the MM-TME in bone marrow and spleen encompassing different stages of disease, using the immunocompetent 5T33MM mouse model. Through comparative analysis, we correlated our murine dataset with the pathogenesis in MM patients by reanalyzing publicly available datasets of human bone marrow samples across various disease stages. Using flow cytometry, we validated the dynamic changes upon disease progression in the 5T33MM model. Furthermore, interesting target populations, as well as the immune-boosting anti-CD40 agonist (αCD40) therapy were tested ex vivo on murine and human primary samples and in vivo using the 5T33MM model.

Results In this study, we identified the heterogenous and dynamic changes within the TME of murine and human MM. We found that the MM-TME was characterized by an increase in T cells, accompanied with an exhausted phenotype. Although neutrophils appeared to be rather innocuous at early disease stages, they acquired a pro-tumorigenic phenotype during MM progression. Moreover, conventional dendritic cells (cDCs) showed a less activated phenotype in MM, underscoring the potential of immune-boosting therapies such as αCD40 therapy. Importantly, we provided the first pre-clinical evaluation of αCD40 therapy and demonstrated successful induction of cDC- and T-cell activation, accompanied by a significant short-term anti-tumor response.

† Kim De Veirman and Damya Laoui have shared senior authorship.

*Correspondence:
Kim De Veirman
Kim.De.Veirman@vub.be
Damya Laoui
dlaoui@vub.be
Full list of author information is available at the end of the article

Conclusions This resource provides a comprehensive and detailed immune atlas of the evolution in human and murine MM disease progression. Our findings can contribute to immune-based patient stratification and facilitate the development of novel and durable (immune) therapeutic strategies in MM.

Keywords Multiple myeloma progression, 5T33MM immune microenvironment, Single-cell RNA-sequencing, Human-mouse comparison, Anti-CD40 agonist therapy

Background

Multiple Myeloma (MM) is an incurable hematological malignancy characterized by the proliferation of clonal, malignant plasma cells within the bone marrow (BM) [1]. Although precursor stages such as monoclonal gammopathy of undetermined significance (MGUS) and smoldering multiple myeloma (SMM) are readily identifiable, active surveillance is the prevailing standard of care until progression to MM [2]. Current therapies for newly diagnosed MM (NDMM) patients comprise autologous stem cell transplantation, proteasome inhibitors, dexamethasone, immunomodulatory drugs and anti-CD38 monoclonal antibodies. Despite high initial response rates, most patients eventually relapse and become multi-refractory. Therefore, novel immunotherapies including bispecific T-cell engagers (directed against BCMA and GPRC5D, markers upregulated on MM cells) and anti-BCMA CAR T-cell therapies are promising new treatment options for relapsed/refractory MM patients [3, 4]. Although these immune-based therapies can induce potent clinical responses in MM, their efficacy often relies on a functional immune microenvironment. Therefore, it remains critical to gain insights into the dynamic changes within the immune cell compartment throughout disease progression, as well as after therapy.

Single-cell RNA-sequencing (scRNA-seq) has significantly advanced our understanding on intra- and inter-tumoral heterogeneity in primary BM samples of MM patients [5, 6]. Recent independent scRNA-seq studies on the BM-TME across distinct stages of disease progression mainly focused on the lymphoid compartment, revealing an increase of natural killer (NK) cells at early stages [7]. Disease progression was further characterized by a decrease in memory and naïve $CD4^+$ T cells [8], accompanied with an enrichment in regulatory T cells (Tregs) [8], an increase in effector $CD8^+$ T cells [7, 8] and the accumulation of $PD1^+$ γδ T cells in relapsed MM patients [6]. Within the myeloid compartment, mature neutrophils were enriched at early stages [9] and disease progression was accompanied by defective antigen presentation by $CD14^+$ monocytes [7], and the accumulation of tumor-associated macrophages (TAMs) in relapsed patients [6]. ScRNA-seq could also identify the enrichment of exhausted $CD8^+$ T cells and 'M2' tolerogenic macrophages as characteristics for rapid progressive disease (RPMM) and a higher enrichment for immature B cells in non-progressive disease (NPMM) [10].

Although these human data are very valuable, important immune cell types, such as dendritic cells (DCs), remain underexplored in MM. Additionally, a full longitudinal follow-up of MM patients along with a comprehensive evaluation of the entire immune microenvironment during disease progression, is still lacking. Moreover, since murine MM models are essential for identifying novel targets and evaluating (new) immunotherapies, it is crucial to investigate and understand the extent to which the immune cell compartment in these models mirrors that of human disease.

To address this, we unraveled dynamic changes in the immune microenvironment using scRNA-seq and multiparameter flow cytometry throughout MM disease progression in the 5T33MM mouse model. The 5T33MM model has been extensively used to study MM pathobiology and to evaluate existing and novel therapies in MM [11]. This model shares many similarities with the human disease including the uncontrolled proliferation of plasma cells in the hematopoietic organs, the presence of M-protein in serum and a disturbance in immune surveillance. Importantly, we correlated our findings with the human disease using publicly available datasets including healthy individuals, MGUS, SMM, full-blown MM and Relapsed/Refractory MM (RRMM) samples [6, 7]. Interestingly, we revealed a high similarity between the human and murine immune compartment upon MM disease progression. We noted an increase in $CD4^+$ T-cells and $CD8^+$ effector memory T-cells, however, this was associated with a significant loss in IFN-γ production, alongside the exhibition of features indicative of an exhausted phenotype. Moreover, we observed in both human and murine MM a shift towards an IFN-associated gene signature in myeloid cells (e.g. neutrophils, monocytes and pDCs). Our scRNA-seq data revealed neutrophils and dendritic cells (DCs) as interesting target populations, however while neutrophil depletion resulted in significant anti-tumor effects at end-stage of disease, anti-CD40 agonist (αCD40) therapy successfully induced cDC- and T-cell activation at earlier timepoints, which also resulted in significant anti-MM effects in the 5T33MM model.

Together, this detailed single-cell atlas of the 5T33MM model, and its direct comparison with human MM, comprise an extensive resource for the exploration of immune targets and cell subsets in MM. Our data clearly demonstrate the similarities and clinical relevance of the 5T33MM model to study MM immunobiology and to evaluate (novel) immunotherapeutic approaches. It thoroughly delineates the transcriptional and compositional alterations occurring in the MM-tumor microenvironment (TME), thus highlighting potential mechanisms of anti-tumor immune responses and immune evasion. Finally, our findings emphasize the overlooked importance of cDCs in anti-MM immune responses, as we present the first pre-clinical evidence supporting the efficacy of αCD40 therapy in MM.

Material and methods

Mice

Six- to eight-week old female C57BL/KaLwRij mice were purchased from Envigo (Horst, The Netherlands). All experimental procedures, follow-up and housing complied with the guidelines of the Belgian Council for Laboratory Animal Science and were approved by the Ethical Committee for Animal Experiments of the Vrije Universiteit Brussel (LA1230281, CEP 19-281-3, CEP 20-281-5, CEP 23-281-5, CEP 23-281-6, CEP 23-281-14).

Tumor model—in vivo experiments

For the 5T33MM model, the 5T33MMvv cell line was derived from aging C57BL/KaLwRij mice which spontaneously developed MM [12]. 5×10^5 cells of the total BM were resuspended in 200 µL RPMI-1640 medium, and intravenously (iv) injected into the tail vein of syngeneic C57BL/KaLwRij mice. At indicated timepoints, the tumor load was assessed (1) by flow cytometry (using the in-house purified anti-idiotype antibody labeled with AF647, using fluorescent protein labeling kits (Thermo Fisher Scientific, Cat.nr. A20173)), (2) by the percentage of plasmacytosis counted on cytospins using May-Grünwald Giemsa staining, and (3) by quantifying M-protein in serum. The M-protein was determined by serum electrophoresis, performed at the UZ Brussels. In addition, the immune cell compartment was evaluated by flow cytometry. Antibodies used for analysis are listed in Supplementary Table S.1.

The idiotype is a clonal immunoglobulin molecule that is expressed by immune cells, typically B cells or plasma cells, and can function as a MM-specific antigen. The anti-idiotype antibody is directed against the M-protein secreted by 5T33MM cells [13].

Cytospin staining and analysis

Cytospins were used to determine the percentage of plasmacytosis in BM and spleen. 1×10^5 cells in 200 µL RPMI-1640, supplemented with 10% (v/v) heat-inactivated fetal calf serum FCS (PAN Biotech, Aidenbach, Bayern, Germany), were centrifuged onto borosilicate glass microscope slides (VWR International, Pennsylvania, US) at 72 g for 7 min. Next, cytospins were stained by May-Grünwald Giemsa staining for manual counting of the percentage plasmacytosis. For each sample, three arbitrary regions of 100 cells were counted per cytospin. The counting was conducted in a blinded fashion to ensure unbiased assessment. Finally, cytospins were scanned using the Leica Aperio GT 450 system and analyzed using the QuPath v0.4.3 software, as illustrated in Supplementary Figure S.1A.

Blood collection and tissue dissociation

Murine blood (approximately 500 µL) was collected retro-orbitally, in a Micro sample tube Serum Gel CAT (Sarstedt AG & Co, Germany), and used to determine the M-protein, as well as for validation of the depletion regimen via flow cytometry. BM was collected by flushing the femur and tibia with a syringe containing RPMI-1640 medium. Spleens were collected and perfused with 800 Units/mL Collagenase III (Gestimed, Oudergem, Belgium), followed by incubation for 20 min at 37 °C and 5% CO_2. Afterwards, the perfused spleens were crushed with the back of a sterile syringe. The single-cell suspensions obtained from indicated tissues were filtered through a sterile 70 µm cell strainer and subjected to Red Blood Cell lysis and counted with Trypan Blue.

In vivo neutrophil depletion

5T33MM-inoculated mice were subjected to a daily intraperitoneal (ip) injection of 75 µg rat IgG2a isotype control (Iso ctrl; clone 2A3; BioXCell) or anti-Ly6G (clone 1A8; BioXCell), followed by 150 µg of anti-Rat (clone MAR18.5; BioXCell) in a volume of 100 µL HBSS, starting at 4 days post-5T33MM inoculation (DPI). This strategy results in efficient depletion of neutrophils as from 6 DPI, which is the time point by which tumor cells have migrated to the hematopoietic tissues and have started initial proliferation. Successful neutrophil depletion was determined by flow cytometry through the comparison of the percentage of $CXCR2^+$ (mainly mature) neutrophils within $CD11b^+$ cells in blood at 4 DPI (before treatment regimen), 6 DPI and 13 DPI, and in BM and spleen at end-stage (20 DPI). At end-stage, mice were sacrificed to assess tumor load and to examine the immune cell compartment.

Ex vivo αCD40 therapy on murine tissue

Total BM and spleen from 5T33MM-inoculated mice were collected and processed to a single-cell suspension at 14 DPI, as previously described. 1×10^6 cells were plated in a 24-well plate in 1 mL RPMI-1640 supplemented with 10% (v/v) heat-inactivated FCS, 2 mM L-glutamine, and 1% penicillin/streptomycin (Thermo Fisher Scientific). Cells were treated with 10 µg rat IgG2a isotype control (Iso ctrl; clone 2A3; BioXCell) or αCD40 therapy (clone FGK4.5/FGK45; BioXCell), and incubated for 24h and 72h at 37 °C and 5% CO_2. The effects on the immune cell compartment and tumor load were analyzed using flow cytometry.

In vivo αCD40 therapy

5T33MM-tumor bearing mice received a single ip injection of 100 µg of rat IgG2a isotype control (Iso ctrl; clone 2A3; BioXCell) or αCD40 therapy (clone FGK4.5/FGK45; BioXCell), in a volume of 100 µL HBSS at 6 DPI. The effects on the immune cell compartment and tumor load were analyzed using flow cytometry.

Flow cytometry

Samples for flow cytometry were washed in PBS, and stained with Fixable Viability Dye eFluor™ 506 (1:1000, eBioscience) for 30 min at 6 °C. Subsequently, cell suspensions were washed and resuspended in PBS supplemented with 2 mM EDTA and 0.5% (v/v) FCS. In order to prevent non-specific binding of antibodies to Fc-receptors, cells were incubated with FcR-blocking Reagent (diluted 1:200; Miltenyi Biotec) for a minimum of 10 min at 6 °C. Next, cells were incubated with the antibody labeling mix diluted in PBS supplemented with 2 mM EDTA and 0.5% (v/v) FCS, for 20 min at 6 °C. Antibodies used for analysis are listed in Supplementary Table S.1 (mouse) and Supplementary Table S.2 (human).

For intra-cellular staining, following the completion of extra-cellular staining, the samples were centrifuged, and fixed using eBioscience™ Intracellular Fixation & Permeabilization Buffer Set (Thermo Fisher Scientific, 88–8824–00) or eBioscience™ Foxp3/Transcription Factor Staining Buffer Set (Thermo Fisher Scientific, 00–5523–00) in accordance with the manufacturer's instructions. For optimal results, incubation of the intracellular staining was essential for the in-house anti-idiotype antibody conjugated with AF647, and the FoxP3 and IFN-γ antibodies, which were incubated for 20 min or overnight at 6 °C, respectively.

To stimulate NK and T cells, and for optimal staining of IFN-γ, single-cell suspensions were pre-incubated in RPMI-1640 medium (Thermo Fisher Scientific, Aalst, Belgium), supplemented with 10% (v/v) heat-inactivated FCS, 300 µg/mL L-glutamine, 100 units/mL penicillin, 100 µg/mL streptomycin, 1 mM non-essential amino acids, 1 mM sodium pyruvate, 0.02 mM 2-mercapto ethanol, 5 µg/mL Brefeldin A (BioLegend), 20 ng/mL phorbol 12-myristate 13-acetate (PMA; Sigma-Aldrich), and 1 µg/mL ionomycin (Invitrogen) for 4 h at 37°C and 5% CO_2.

To assess In vitro cell proliferation, cells were labeled using the CellTrace™ CFSE Cell Proliferation Kit (Invitrogen, Thermo Fisher Scientific, C34554), as previously described [14].

To assess the anti-tumor effects upon therapy in primary human BM samples, cells were stained with PI (BioLegend, 421,301) and CD138-APC (clone; DL-101, BioLegend).

Flow cytometry data were acquired using the BD LSR-Fortessa (BD Biosciences) and analyzed using FlowJo v10.8.1.

Fluorescence-activated cell sorting (FACS)

Naïve and 5T33MM-inoculated mice were sacrificed at 14 DPI and 20 DPI, with four mice pooled for each condition. The standard tissue dissection and processing protocols were conducted with the addition of actinomycin D (ActD, Sigma-Aldrich, A1410-5MG) in each buffer. BM and spleen collection was performed in the presence of 30 µM ActD, and all subsequent steps in the presence of 3 µM ActD. Next, murine BM and spleen single-cell suspensions were stained with the following fluorochrome-conjugated antibodies; anti-idiotype (in-house)—IgG1-APC, CS1-PE (clone; 4G2, BioLegend), CD45-APC/Cy7 (clone: 30-F11, Biolegend), and 7-AAD (BD Biosciences). $CD45^+$ $idiotype^-/CS1^-$ $7\text{-}AAD^-$ cells were sorted into PBS + 0.04% UltraPURE BSA (UltraPureTM Bovine Serum Albumin (BSA, 50 mg/mL) Thermo Fisher Scientific), and used for single-cell RNA-sequencing. FACS was conducted with the BD FACSAria™II (BD Biosciences).

Single-cell RNA-sequencing (scRNA-seq) using the 10 × Genomics platform

BM and spleen single-cell suspensions from each indicated time point during MM progression (Naïve, 14 DPI, and 20 DPI) were loaded as separate samples on a Chromium Controller (10 × Genomics) to generate single-cell gel beads in emulsion (GEM). GEMs and scRNA-seq libraries were prepared using a Chromium Next GEM Single Cell 3′ GEM, Library & Gel Bead Kit v3.1 and a Chromium i7 Multiplex kit (10 × Genomics, CG000204) according to the manufacturer's instructions. Briefly, GEM reverse-transcription incubation was performed in a thermal cycler at 53 °C for 45 min, 85 °C for 5 min and ending at 4 °C. Next, GEMs were broken and complementary DNA (cDNA) was cleaned up using DynaBeads

MyOne Silane Beads (ThermoFisher Scientific, 37002D) and SPRIselect Reagent kit (Beckman Coulter, B23318). Full-length, barcoded cDNA originating from the mRNA was PCR amplified with a 96-deep-well reaction module at 98 °C for 3 min, 14 cycles at 98 °C for 15 s, 67 °C for 20 s and 72 °C for 1 min, 1 cycle at 72 °C for 1 min and ending at 4 °C. Size selection via a SPRIselect Reagent kit was used to separate the amplified cDNA molecules for 3′ gene expression library construction. Gene expression library construction to generate Illumina-ready sequencing libraries was performed after clean-up using a SPRIselect Reagent kit and enzymatic fragmentation by adding R1 (read 1 primer), P5, P7, i7 sample index and R2 (read 2 primer sequence) via end-repair, A-tailing, adapter ligation, post-ligation SPRIselect clean-up/size selection and sample index PCR. The cDNA content of pre-fragmentation and post-sample index PCR samples was analyzed using a 2100 BioAnalyzer (Agilent). Simultaneously generated (14 DPI and Naïve, and 20 DPI) 10X v3.1 cDNA-libraries were equimolarly pooled. Pools were purified with 1.2 volumina AMPure XP Beads and sequenced on Illumina NovaSeq 6000 (Paired End Read) with 10X v3 settings: Read1: 28 cycles / i7 index: 8 cycles / i5 index: 0 cycles / Read 2: 91 at the VIB Nucleomics Core (https://nucleomicscore.sites.vib.be/en).

ScRNA-seq data processing

Cell Ranger software v.6.1.2 from 10×Genomics was used for alignment of the RNA sequencing reads to the mm10 genome (v. mm10-2020-A), barcode processing, unique molecular identifiers filtering and single-cell Unique Molecular Identifier (UMI) counting. The average mean number of mapped RNA reads per cell was 46.387 ± 9.544 SE, with an average sequencing saturation metric of 62.53% ± 5.85% SE. Further pre-processing and analysis of the UMI count matrices were performed in R using Seurat v4.0.5, DropletUtils v1.10.3, scater v1.18.3, scDblFinder v1.4.0. The cellular barcodes, associated with low quality "empty" droplets, were filtered out using the "emptyDrops" function of the DropletUtils package with the recommended FDR cut-off < = 0.1 for deviation from the ambient RNA profile. Outlier cells were additionally identified based on library size, number of expressed genes and mitochondrial proportion per cell; cells were tagged as outliers and removed, when they were more than three median absolute deviations distant from the median value of each metric across all cells, or if they exceeded 20% of mitochondrial genes per cell. Low-abundance genes were removed based on the distribution of the mean counts per gene for each sample, following the proposed Bioconductor workflow [15]. A doublet score was assigned to each cell barcode based on the generation of cluster-based artificial doublets with the scDblFinder function of the scDblFinder package. The gene expression matrices were further normalized, and scaled, followed by the selection of highly variable genes (HVG), principal component analysis (PCA), and unsupervised clustering using Seurat. The genes, specifically expressed in each cluster, were identified via differential expression (DE) analysis with the "FindMarkers" function of Seurat (Wilcoxon Rank Sum test). The p-values of DE were adjusted for multiple testing with Bonferroni correction. Clustering results were visualized with two-dimensional scatter plots using the Uniform Manifold Approximation and Projection (UMAP) dimensionality reduction method. We excluded cell populations that showed both high doublet score and expression of markers, specific for two different cell types. Additionally, we excluded clusters that were outliers due to low library size and number of expressed genes, and that lacked a distinct gene signature compared to the other clusters.

Several of the identified immune compartments, including NK-/T-cells, myeloid cells and DCs, were individually further subclustered in order to obtain a more refined mapping of the immune subpopulations in MM. The processing of the subsets was the same as described above, with the exception of the DC compartment, where we regressed out a proliferation gene signature from the expression matrix during data scaling. The CellCycleScoring Seurat function was used to assign a score to each cell based on known G2/M and S phase markers. Then, the G2M and S scores were regressed out and used further for dimensionality reduction.

Publicly available human MM scRNA-seq datasets

Zavidij et al. generated a scRNA-seq dataset of the $CD138^{-}CD45^{+}$ sorted immune cell compartment of primary BM samples derived from patients with MGUS (n = 5), SMM (n = 11; including low-risk/high-risk SMM), and NDMM (n = 7), as well as healthy individuals (n = 9) [7]. The sample processing procedure was described as follows: $CD138^{-}$ or $CD45^{+}$ BM cell fractions were isolated using magnetic activated cell sorting (MACS, Miltenyi Biotec). The selected cells were either cryopreserved in 10% dimethyl sulfoxide (DMSO) or immediately processed for scRNA-seq. Tirier et al. generated a scRNA-seq dataset of the $CD138^{-}$ sorted immune cell compartment in primary BM samples derived from RRMM patients (n = 20) [6]. The sample processing procedure was described as follows: BM aspirates were subjected to mononuclear cell separation by density centrifugation, red blood cells lysis, MACS with anti-CD138 microbeads (Miltenyi Biotec), and frozen in 90% FCS (Sigma-Aldrich) supplemented with 10% DMSO (Serva Eletrophoresis) for storage in liquid nitrogen until further use. We extracted the gene expression count matrices and

cellular metadata of both datasets from the GSE124310 and GSE161801 GEO accessions, respectively. All non-immune cells, platelets and MM cells were removed from the dataset for better comparability with the mouse scRNA-seq dataset.

The two datasets from GSE124310 and GSE161801 were merged, followed by normalization, scaling, selection of HVG and PCA. Only HVG present in both datasets were included in the PCA. To remove batch effects between the two datasets, we applied the algorithm from the Harmony R package v1.2.0 with the theta parameter set to one. Higher values of theta favor higher diversity of batches in the clusters and result in stronger alignment. Then, the corrected Harmony embeddings were used to perform unsupervised clustering of the cells and UMAP dimensionality reduction. For the comparison of the murine MM neutrophils with their human counterparts, the scRNA-seq dataset from de Jong et al. [9] was reanalyzed, containing human BM neutrophils from healthy individuals, NDMM and treated MM patients. Expression data was assessed through Mendeley Data (https://data.mendeley.com/datasets/sm7fvt8hsg), by downloading the integrated neutrophils_controlNDMM.rds and neutrophils_controlTMM.rds files. The neutrophils from healthy individuals, NDMM and treated MM conditions were integrated and processed as described above for GSE124310 and GSE161801. Cluster names were assigned based on expression of marker genes (MS4A3, MPO, ELANE, FCN1 for myelocytes; LCN2, LTF, CAMP, MMP8 for Pre-Neu; MMP8, MMP9, S100A8, S100A4 for ImmNeu; G0S2, FCGR3B, CSF3R, TREM1 for MatNeu). A contaminating cluster of doublets with monocytes (CD74, MAFB, THBS1, ZEB2) and erythrocytes (HBA1, HBB) were removed.

Neutrophil maturation status

The signature score for neutrophil maturation was assigned based on the top 50 DEGs between mature and immature neutrophils, as listed in Xie et al. [16]. The signature score was calculated per cell using the AddModuleScore function of Seurat, which yields the average expression level of the signature genes subtracted by the aggregated expression of a control gene set.

Software

Flow cytometry data was analyzed using FlowJo™ v.10.8.1. scRNA-seq datasets were analyzed and graphs were generated using Cell Ranger v.6.1.2, R v.4.2.3, Seurat v.4.0.5 and v.5.0.1, DropletUtils v1.10.3, scater v.1.18.3, scDblFinder v.1.4.0, harmony v. 1.2.0, nichenetr v.2.0.4. All schematic illustrations were generated using BioRender.com.

Statistics

Statistical analyses were performed using GraphPad Prism 10.2.2 software. For pairwise comparisons, the one-tailed unpaired Mann–Whitney U-test was used. For multiple group comparisons, the one-way ANOVA test was used. Tumor load and immune kinetics were compared by two-way ANOVA with multiple comparisons tests. All graphs show mean with SD. Differences with a $p < 0.05$ were considered statistically significant; $^{*}p < 0.05$, $^{**}p < 0.01$, $^{***}p < 0.001$, and $^{****}p < 0.0001$.

Results

A detailed atlas of the tumor-immune microenvironment in murine and human MM

To investigate the dynamic changes within the MM-TME, we used the immunocompetent 5T33MM mouse model. Tumor progression was monitored in the BM, spleen and serum at 7, 14, and 20 DPI, the latter corresponding to end-stage of disease with mice showing signs of paralysis, and compared to naïve control mice (Fig. 1A, Supplementary Figure S.1A–B). In both BM and spleen, the increase in tumor load, demonstrated by an increase in plasmacytosis and M-protein (Fig. 1A), was associated with a significant decrease in the percentage of $CD45^{+}$ immune cells as from 14 DPI (Supplementary Figure S.1C). Notably, in the spleen, the absolute number of $CD45^{+}$ immune cells increased until 14 DPI when compared to naïve mice, suggesting immune infiltration in the first phases of tumor progression (Fig. 1B).

To dissect how the immune TME changes upon MM disease progression, we performed scRNA-seq on fresh $CD45^{+}$idiotype^{-} immune cells using the 10×Genomics platform on BM and spleen samples from naïve, 14 DPI and 20 DPI 5T33MM-bearing C57BL/KaLwRij mice (Fig. 1C). Unsupervised clustering, dimensionality reduction and UMAP were performed on 47.129 cells (Fig. 1D). Individual clusters were identified based on the expression of known marker genes (Supplementary Figure S.1D). Our scRNA-seq data revealed the heterogenous myeloid and lymphoid compartment within the BM and spleen, thereby identifying at least 17 cell types and progenitor cells (Fig. 1D). Among the myeloid cells, which mainly derived from the BM samples, precursors, DC-precursors, monocytes, and neutrophils were the most abundant populations. The lymphoid cells included NK-/T-cells and B cells, and were more abundant in the spleen (Fig. 1D-E). Importantly, our scRNA-seq dataset unveiled the dynamic changes in the composition of various cell types at different stages of MM disease progression (naïve, 14 DPI and 20 DPI) (Fig. 1F-G). In the BM, the B-cell compartment was strongly reduced in MM-bearing mice as compared to naïve mice, while

precursors (including DC precursors and Neu precursors), conventional dendritic cells (cDCs), natural killer T (NKT) and T cells increased. Similar but less pronounced trends were observed in the spleen, however, in contrast to the BM, neutrophils increased in the spleen upon tumor progression (Fig. 1G). Of note, within the B-cell compartment, we identified a small fraction of plasma cells, which poorly expressed the MM marker *Tnfrsf17*, indicating that our dataset is only minimally contaminated with MM cells (Supplementary Figure S.1E and F). We further validated these kinetic changes observed in scRNA-seq by flow cytometry, using the gating strategy illustrated in Supplementary Figure S.1G, in naïve and 5T33MM-bearing mice at 7, 14 and 20 DPI. Overall, similar alterations were observed in the distinct immune cell types (Fig. 1H).

To address the current need for a comprehensive understanding of dynamic changes within the immune cell compartment during MM disease progression, and to assess the translatability of our pre-clinical mouse model, we correlated the results obtained from the murine 5T33MM model with publicly available scRNA-seq datasets [6, 7] of healthy donors (n = 9), and MM patients at different stages of the disease, being MGUS (n = 5), SMM (n = 11; including low-risk/high-risk SMM), NDMM (n = 7), and RRMM (n = 20) patients (Fig. 1I). We reanalyzed the $CD45^+CD138^-$ immune compartment, devoid of cancer cells, and identified 15 broad cell types; ranging from precursor cells to myeloid cells (monocytes, macrophages, DCs), lymphoid cells (B-/NK-/NKT-/T-cells), but also erythroid cells and mast cells (Fig. 1J, Supplementary Figure S2A–C). Similar to our murine data, we observed an increase in cDCs, $CD8^+$ T cells, NK cells and NKT cells upon MM disease progression (Fig. 1K). Intriguingly, BM-precursor cells increased in mouse, while a decrease could be observed in human samples at all stages of disease progression. Of note, the kinetic human scRNA-seq dataset does not contain neutrophils. This could be due to the low transcript counts in neutrophils, due to the use of density gradients during sample processing or due to the fact that the sequencing was performed on frozen patient samples [17].

In conclusion, temporal analysis of the dataset we generated allows us to track the evolution of the immune TME and identify key changes associated with disease progression in both murine and human MM.

The MM microenvironment is characterized by the presence of T cells with an exhausted phenotype

T cells are major players in adaptive immunity and are essential for mounting an effective anti-tumor immune response [18, 19]. Therefore, we delved deeper into the NK-/T-cell compartment and upon subclustering, we could distinguish at least 14 distinct cell types based on signature and activation genes (Fig. 2A, Supplementary Figure S.3A). The annotation of the distinct clusters was validated by the alignment of our murine scRNA-seq data with the tumor-infiltrating T-cell atlas of Andreatta et al. [20] (Supplementary Figure S.3B).

Unique to our scRNA-seq data is the ability to track the evolution of the different T-cell subsets within the MM-TME (Fig. 2B, Supplementary Figure S.3C and D). Within the T cells, a clear shift from naïve-like to activated/effector T cells was observed in MM-bearing mice when compared to naïve mice (Fig. 2B). As such, in the 5T33MM model, we observed a decrease in CD4_Naïve-like and CD8_Naïve-like clusters, which were marked by a high expression of *Ccr7*, *Sell* (encoding for CD62L), *Tcf7* and *Lef1*, and corresponded to naïve and/or central memory T-cells [21] (Supplementary Figure S.3A). In addition, the CD8_Effector memory, CD8_IFN and T_Prolif cluster were defined based on the expression of genes

(See figure on next page.)

Fig. 1 A detailed atlas of the tumor-immune microenvironment in murine and human MM. (**A**) Bar graphs show the tumor load in the 5T33MM bone marrow (BM), spleen and serum at 7, 14, and 20 days post-tumor inoculation (DPI). This is demonstrated by the percentage of plasmacytosis in BM and spleen, and the presence of the M-protein (g/L) in serum. (**B**) Bar graphs show the absolute number of $CD45^+$ cells in BM and spleen of naïve and 5T33MM mice at 7, 14, and 20 DPI. n = 5 per group. (**C**) Schematic outline of the experimental procedures, detailing the sorting of 7-AAD^-CD45^+idiotype$^-$ immune cells from naïve and 5T33MM mice (at 14 DPI and 20 DPI) for single-cell RNA-sequencing (scRNA-seq; 10 × Genomics). n = 4 samples pooled. (**D**) UMAP plot shows high-resolution clustering of the immune cell compartment in BM and spleen, using the scRNA-seq dataset of naïve mice and the 5T33MM model. (**E**–**F**) UMAP embedding as shown in panel D, but colored according to (E) tissue of origin; including BM and spleen, and (F) stage of disease; including naïve mice and 5T33MM mice at 14 DPI and 20 DPI. (**G-H**) Bar graphs show the frequency of immune cells within the $CD45^+$ cells across different stages of disease in murine BM and spleen, analyzed using (G) scRNA-seq and (H) flow cytometry. (**I**) Schematic outline of the consulted publicly available datasets (scRNA-seq; 10 × Genomics), including a $CD138^-CD45^+$ sort on mononuclear cells from healthy individuals (n = 9), precursor stages such as Monoclonal Gammopathy of Undetermined Significance (MGUS; n = 5) and Smoldering Multiple Myeloma (SMM; n = 11), as well as Newly Diagnosed Multiple Myeloma (NDMM; n = 7) and Relapsed/Refractory Multiple Myeloma (RRMM; n = 20). (**J**) UMAP plot shows high-resolution subclustering of the immune cell compartment within the human BM scRNA-seq dataset. (**K**) Bar graph shows the frequency of immune cells within the $CD45^+$ cells of the human BM scRNA-seq dataset across different stages of disease. Error bars represent mean values ± SD. Statistical analysis was performed by Ordinary One-way ANOVA. ns: $p \geq 0.05$, *$p < 0.05$, **$p < 0.01$, ***$p < 0.001$, and ****$p < 0.0001$

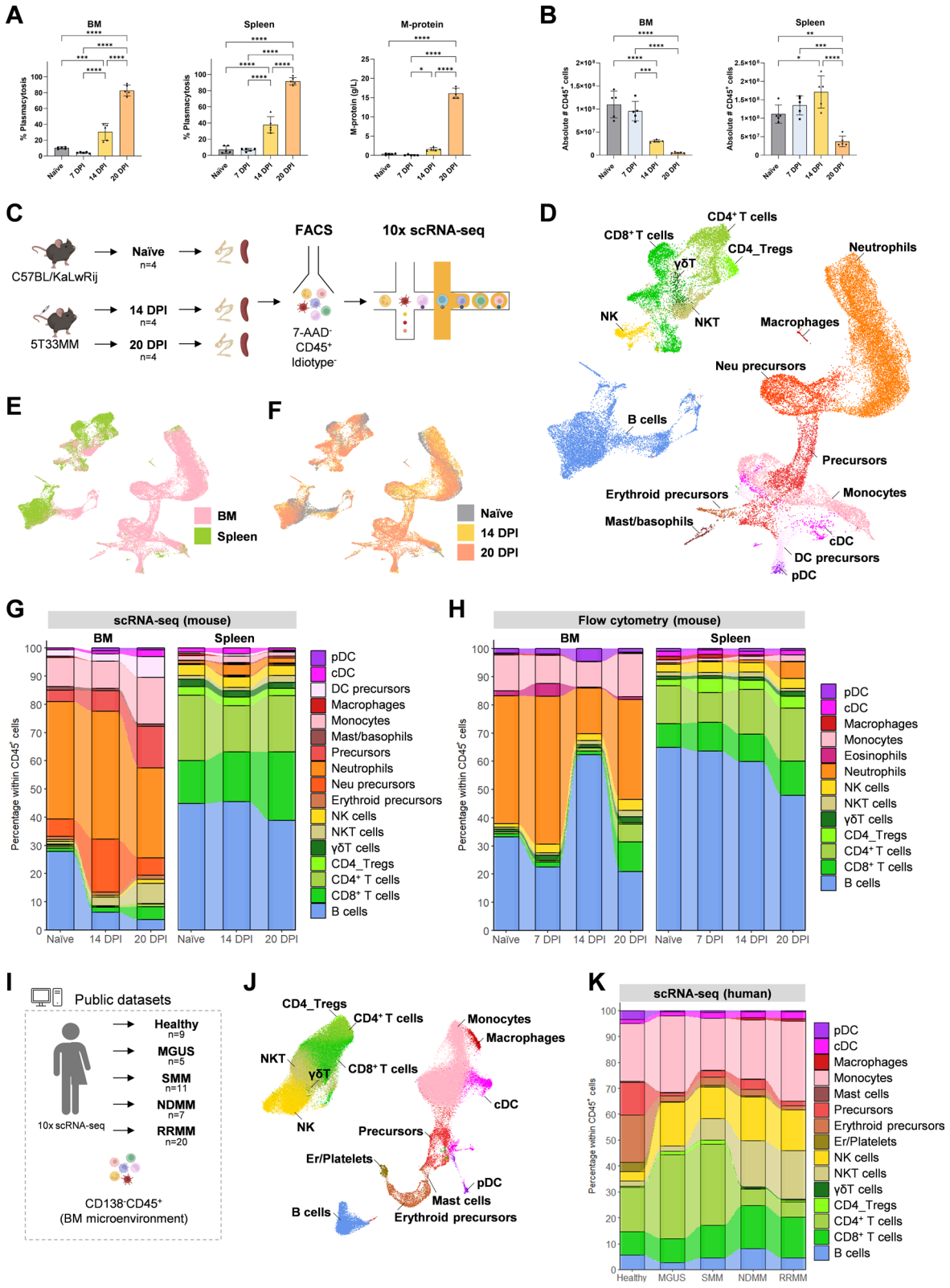

Fig. 1 (See legend on previous page.)

associated with effector CD8$^+$ T-cells (*Gzmb*, *Gzma*, *Gzmk*, *Prf1*, *Ifng*), IFN-associated genes (*Ifit3*, *Isg15*, *Ifit1*, *Stat1*, *Rsad2*) and cell-cycle genes (*Mki67*, *Top2a*, *Stmn1*) respectively, and drastically increased upon disease progression (Fig. 2B, Supplementary Figure S.3A). Other changes induced by the disease were the radical decrease in γδT cells, a slight decrease in Tregs and NK cells, and an important increase in NKT cells in the BM (Fig. 2B).

Next, we aimed to validate the changes in the NK-/T-cell compartment using flow cytometry and confirmed that, although the absolute numbers of each lymphoid cell type was significantly decreased upon disease progression (Supplementary Figure S.4A and B), the proportion of CD4$^+$ T, CD8$^+$ T, as well as Tregs significantly increased within the NK-/T-cell compartment of MM-bearing mice (Fig. 2C), though overall the CD8$^+$ T/Treg ratio was decreased in MM-bearing mice compared to naïve mice (Fig. 2D). Similar to what was observed in the scRNA-seq dataset, we observed a significant increase in CD62L$^-$CD44$^+$ effector memory CD4$^+$ T cells in the spleen, and CD8$^+$ T cells in the BM and spleen, upon MM disease progression using flow cytometry (Fig. 2E, Supplementary Figure S.4C–F). However, when further looking into the functional state of several effector cells (NK-, NKT-, and CD4$^+$ and CD8$^+$ T-cells), we found that their potency to produce IFN-γ was significantly decreased in end-stage 5T33MM mice (Fig. 2F, Supplementary Figure S.5A and B). These findings suggest an impaired T-cell function, especially at end-stage of disease. Indeed, at the transcriptome level, we observed a higher expression of exhaustion/dysfunction markers such as *Tox*, *Havcr2*, *Vsir*, *Lag3*, *Ctla4*, *Pdcd1* in the 5T33MM model (Supplementary Figure S.5C). Moreover, within the effector cluster, the exhausted CD4$^+$ T cells (CD4_Exhausted) and CD8$^+$ T cells (CD8_Exhausted) were exclusively present in MM-bearing mice and increased upon MM disease progression from 14 to 20 DPI, and were absent in naïve mice (Fig. 2G-H, Supplementary Figure S.5D). Accordingly, a significant increase of PD1 in CD4$^+$ and CD8$^+$ T cells was observed at the protein level in end-stage 5T33MM mice (Supplementary Figure S.5E and F).

Within the human scRNA-seq dataset, the CD4$^+$ T cells showed a slight increase in precursor stages of the disease (MGUS and SMM), however, once progressing to MM (NDMM), CD4$^+$ T cells were strongly decreased and remained low in RRMM (Fig. 1K, Supplementary Figure S.2C). While CD8$^+$ T cells showed minimal variation throughout disease progression, NKT cells were enriched in NDMM and RRMM, when compared to healthy individuals and precursor stages (Fig. 1K, Supplementary Figure S.2C). Upon subclustering the NK-/T-cells in the human scRNA-seq dataset, we were able to identify similar activation states based on shared DE genes between mouse and human (Fig. 2I, Supplementary Figure S.6A–C). Interestingly, an increase in the CD8_IFN cluster could be observed in NDMM and RRMM patients compared to healthy controls (Fig. 2J, Supplementary Figure S.6A). Similar to our murine dataset, T cells from NDMM and RRMM patients also showed an increase in the expression of exhaustion markers, thus indicative of an exhausted phenotype (Supplementary Figure S.6D and E). Hence, despite the presence of effector cells, their function may be impaired in NDMM and RRMM, potentially leading to unsuccessful tumor control.

In conclusion, our data showed strong alignments within the NK-/T-cell compartment between both species, including an increase in effector cells upon MM disease progression, accompanied by an increase in T cells with an exhausted phenotype.

(See figure on next page.)

Fig. 2 The MM microenvironment is characterized by the presence of T cells with an exhausted phenotype. (**A**) UMAP plot shows high-resolution subclustering of the NK-/T-cell compartment within the in-house murine scRNA-seq dataset. (**B**) Bar graph shows the frequency of the different NK-/T-cell subsets within the murine BM and spleen, and across different disease stages; including naïve mice and 5T33MM mice at 14 DPI and 20 DPI, analyzed in the murine scRNA-seq dataset. (**C** and **D**) Bar graphs show (C) the frequencies of CD8$^+$ T cells, CD4$^+$ T cells, Foxp3$^+$ T cells, γδT cells, NKT cells and NK cells as a percentage of the NK and T cells (CD11b$^-$ CD19$^-$ cells), and (D) the CD8$^+$ T cells/Treg ratio in BM (top) and spleen (bottom) from naïve and 5T33MM mice at 7, 14, and 20 DPI. Analyzed using flow cytometry. n = 5 per group. (**E**) Bar graph shows the frequency of CD44$^+$CD62L$^+$ Central memory T cells, CD44$^-$CD62L$^-$ T cells, CD62L$^+$CD44$^-$ Naïve T cells and CD62L$^-$CD44$^+$ Effector T cells within the CD8$^+$ T cells in murine BM and spleen, and across different stages of disease, analyzed using flow cytometry. n = 5 per group. (**F**) Bar graphs show ΔMFI (median fluorescence intensity) of IFN-γ in CD4$^+$ T cells and CD8$^+$ T cells present in the BM and spleen across different stages of disease, analyzed using flow cytometry. n = 5 per group. (**G**) UMAP plot shows high-resolution subclustering of the CD8_Effector memory cluster and the CD4_T cluster, identifying the CD4_Exhausted cluster and the CD8_Exhausted cluster as well as their evolution across different stages of disease, analyzed in the murine scRNA-seq dataset. (**H**) Dot plot shows the expression of marker genes associated with exhaustion within the murine scRNA-seq dataset. Dot size represents the percentage of cells expressing the gene and color gradient represents the average scaled expression within a cell cluster. (**I**) UMAP plot shows high-resolution subclustering of the NK-/T-cell compartment within the human BM scRNA-seq dataset. (**J**) Bar graph shows the frequency of the different NK-/T-cell subsets within the human BM scRNA-seq dataset across different stages of disease. Error bars represent mean values ± SD. Statistical analysis was performed by Ordinary One-way ANOVA. ns: $p \geq 0.05$, *$p < 0.05$, **$p < 0.01$, ***$p < 0.001$, and ****$p < 0.0001$

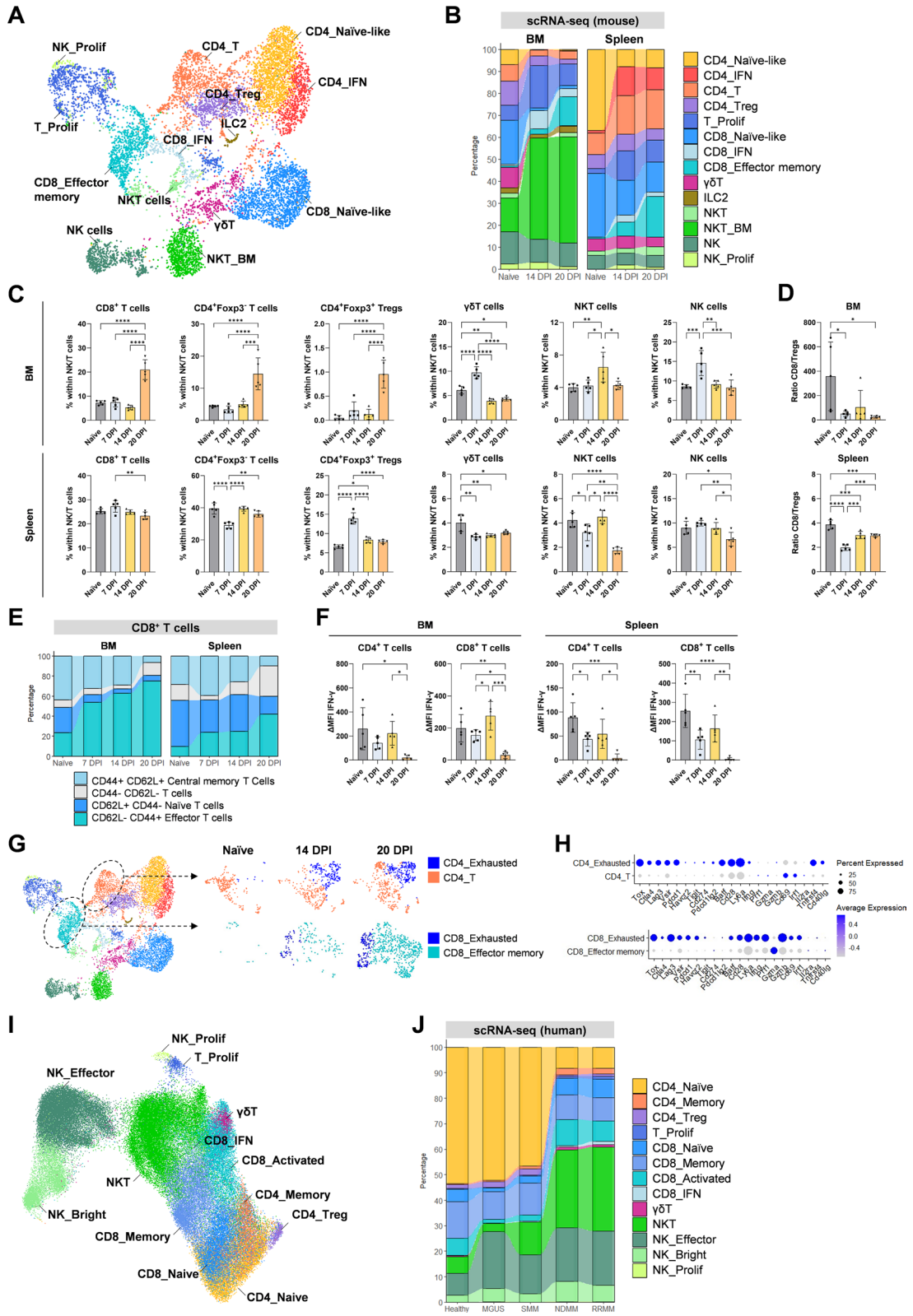

Fig. 2 (See legend on previous page.)

Neutrophils acquired a more pronounced pro-tumor phenotype upon MM disease progression

T cells can be directly suppressed by myeloid cells, which hence contribute to the immunosuppressive microenvironment in MM, thereby impeding the success of current immunotherapeutic approaches [14, 22]. Subclustering of the murine neutrophil and macrophage lineage, revealed 8 distinct clusters, based on specific marker genes, including granulocyte-monocyte progenitors (GMP) that can give rise to monocyte precursors (MP), monocytes and macrophages, and granulocyte precursors (GP) that give rise to neutrophils (Fig. 3A, Supplementary Figure S.7A).

In mice, based on prototypical signature genes, we identified a classical monocyte cluster (Mono_CM; *Ccr2*^{high} and *Cx3cr1*^{low}), and a non-classical monocyte cluster (Mono_NCM cluster; *Ccr2*^{low} and *Cx3cr1*^{high}), the latter being mainly restricted to the naïve condition (Fig. 3A-B, Supplementary Figure S.7A–C). In human, monocytes were subdivided in three clusters: classical monocytes (Mono_CM; CD14^{++}CD16^{-}), intermediate monocytes (Mono_IM; CD14^{++}CD16^{+}), and non-classical monocytes (Mono_NCM; CD14^{+}CD16^{++}) (Supplementary Figure S.8A–D). The Mono_CM cluster and Mono_IM cluster aligned with the murine Mono_CM cluster (expressing *Ccr2*). An additional monocyte cluster, the Mono_IFN cluster, which highly expresses IFN-associated genes, was found in both mouse and human datasets, and was slightly increased in NDMM and RRMM patients (Fig. 3B, Supplementary Figure S.8B and C). Furthermore, macrophages, expressing high levels of *C1qa*, *Maf*, *Ctsd*, and *Mertk*, were strongly reduced in MM-bearing mice, when compared to naïve mice, whereas, in human, macrophages were increased in NDMM and RRMM patients when compared to healthy individuals and precursor stages of MM (Fig. 3B, Supplementary Figure S.7D, Supplementary Figure S.8B and C). Finally, neutrophils, expressing high levels of *Csf3r*, *Cxcr2, Mmp8, Mmp9* and *Ly6g,* represented the most dominant myeloid cell type within the TME of MM-bearing mice. In addition, neutrophil precursors showed a transient expansion during tumor progression (Fig. 3A-B). Although neutrophils were slightly decreased in BM, we observed a major increase in spleen (Fig. 3A-B), which was also confirmed by flow cytometry at end-stage of disease (Fig. 3C).

Given that neutrophils are such a predominant cell population in the BM and have been shown to suppress T cells in tumors [22, 23], we aimed to assess whether neutrophils influenced T-cell numbers and activation status in MM, by use of neutrophil-depleting agents. A daily injection of alternating anti-Ly6G/Isotype and anti-Rat (MAR18.5) in the 5T33MM mice from 4 DPI till end-stage resulted in successful depletion of mature neutrophils in blood, BM and spleen of MM-bearing mice (Fig. 3D, Supplementary Figure S.9A and B). Neutrophil depletion within the 5T33MM model resulted in a significant reduction in tumor burden solely in the BM (Fig. 3E), which is the organ that contains the highest number of neutrophils (Fig. 1G-H). While neutrophil depletion did not affect the frequencies of CD8^{+} or CD4^{+}Foxp3^{-} T cells, it did lead to a significant reduction in CD4^{+}Foxp3^{+} Tregs and a higher activation of CD8^{+} T cells in the BM (Supplementary Figure S.9C and D). These results suggest that neutrophils might have an immunosuppressive or tumor-promoting phenotype.

To assess how the neutrophil phenotype changes with tumor progression, we further subclustered the neutrophils from the murine scRNA-seq dataset and annotated four neutrophil subclusters (Neu1, Neu2, Neu3, Neu4), which aligned with an increasing maturation status (based on Xie et al. [16]), as well as a pronounced

(See figure on next page.)

Fig. 3 Neutrophils acquired a more pronounced pro-tumor phenotype upon MM disease progression. (**A**) UMAP plot shows high-resolution subclustering of the myeloid compartment within the murine scRNA-seq dataset. (**B**) Bar graph shows the frequency of the different myeloid subsets within the murine BM and spleen across different disease stages, including naïve mice and 5T33MM mice at 14 DPI and 20 DPI, analyzed using the murine scRNA-seq dataset. (**C**) Bar graphs show the frequency of neutrophils within the CD11b^{+} cells in the murine BM (top) and spleen (bottom) across different stages of disease, analyzed using flow cytometry. n = 5 per group. Statistical analysis was performed by an Ordinary One-way ANOVA. (**D**) Schematic outline of the experimental procedures. 5T33MM-inoculated mice received alternating anti-Ly6G and anti-Rat (MAR18.5), starting at 4 DPI. Mice were sacrificed at end-stage. (**E**) Bar graphs show the tumor load, assessed by the percentage plasmacytosis in BM and spleen, and via the M-protein in serum. n = 3–4 per group. Statistical analysis was performed by Mann-Whitney U-test. (**F**–**L**) Reclustering of the neutrophils using (**F**–**I**) the in-house murine scRNA-seq dataset, and (**J**–**L**) the human scRNA-seq dataset, based on de Jong et al. [9] (**F**, **J**) UMAP plot shows high-resolution subclustering of neutrophils and neutrophil precursors, analyzed in (F) the murine and (J) the human scRNA-seq dataset. (**G**) Violin plot shows the maturation status of the different neutrophil clusters. The maturation status was determined by the top 50 differentially expressed genes, based on X*ie* et al. [16] (**H**, **K**) Bar graph shows the frequency of the different neutrophil clusters across different stages of disease, analyzed using (**H**) the in-house murine scRNA-seq dataset, and (**K**) the human scRNA-seq dataset. (**I**, **L**) Heatmap plot shows the expression of IFN-associated genes by the different neutrophil clusters across different disease stages, analyzed using (**I**) the in-house murine scRNA-seq dataset and (**L**) the human scRNA-seq dataset. Error bars represent mean values ± SD. ns: $p \geq 0.05$, *$p < 0.05$, **$p < 0.01$, ***$p < 0.001$, and *****$p < 0.0001$

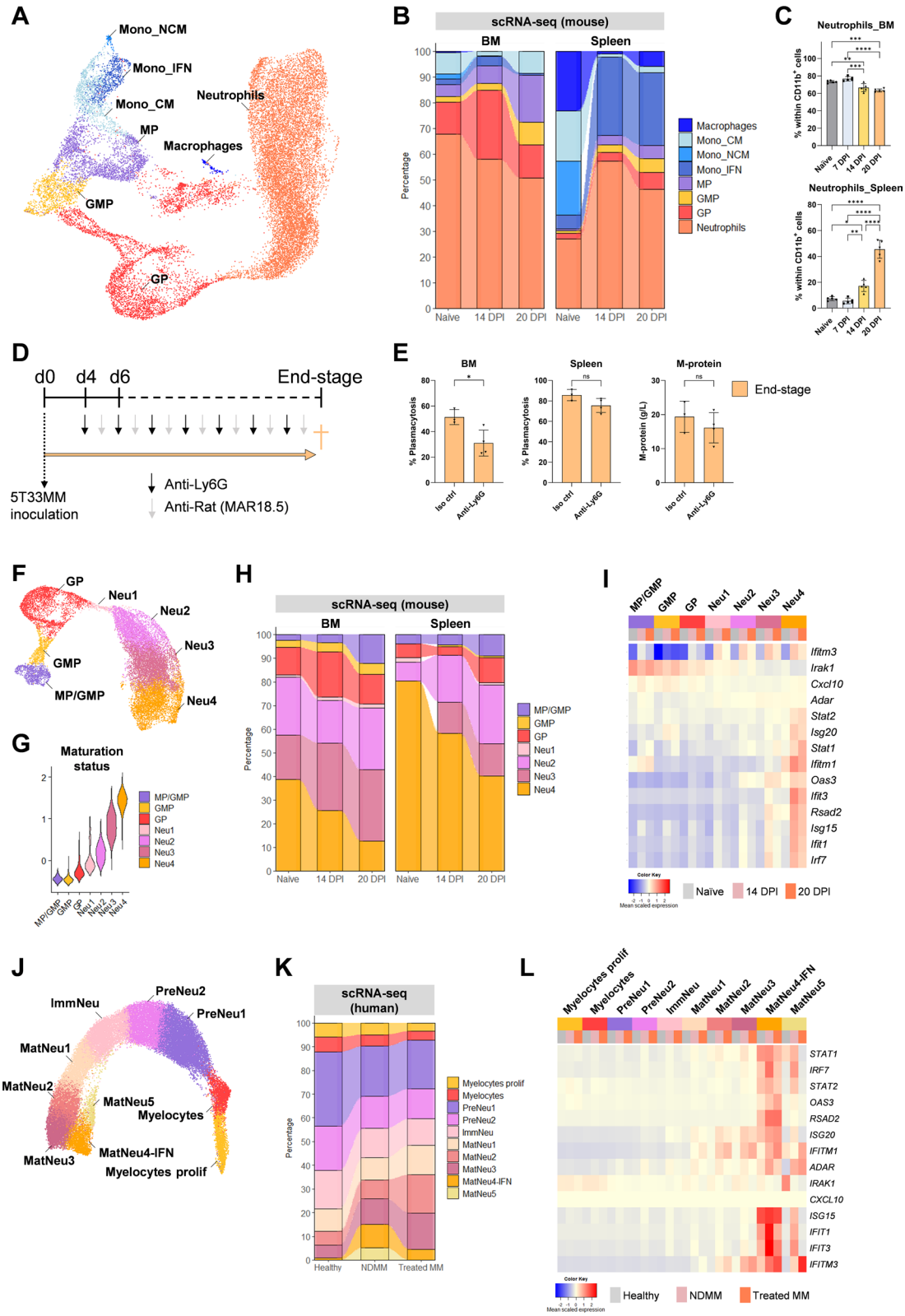

Fig. 3 (See legend on previous page.)

IFN-associated signature (*Ifit1*, *Ifit2*, *Ifit3*, *Ifitm3*, *Rsad2*, *Isg15*) (Fig. 3F-I, Supplementary Figure S.9E–G). Interestingly, less mature or immature neutrophils (e.g. Neu2 and Neu3) were increased in MM-bearing mice compared to naïve mice (Fig. 3H). In addition, tumor progression was accompanied with a decrease in the most mature neutrophils (Neu4), which showed a pronounced IFN-signature at 14 DPI, but decreased expression of IFN-associated genes at end-stage of the disease (Fig. 3H-I). We assessed several functionally relevant genes in neutrophils, and found that in the different neutrophil clusters, most genes associated with neutrophil function and maturation including phagocytosis, chemotaxis, NETosis and granule formation, were expressed to a lower level in MM-bearing mice compared to naïve mice (Supplementary Figure S.9H). Overall, our data suggests that less mature neutrophils infiltrate the TME upon tumor-progression, which might lead to a more immunosuppressive environment.

To assess the translational value of our findings, we reanalyzed the scRNA-seq dataset generated by de Jong et al. [9] on human BM neutrophils from healthy individuals, NDMM and treated MM patients. We successfully aligned the neutrophil substates identified in our murine dataset with those found in the human dataset, which included precursors cells (myelocytes prolif, myelocytes, PreNeu1, PreNeu2), immature neutrophils (ImmNeu) and mature neutrophils (MatNeu1 to 5) (Fig. 3J-K). Consistent with our mouse data, human mature neutrophils in NDMM patients showed an upregulated IFN-associated signature compared to healthy individuals (Fig. 3L). Furthermore, the MatNeu4-IFN cluster (*RSAD2*, *ISG15*, *IFIT1*) was significantly increased in NDMM compared to healthy individuals. However, in contrast to our murine data, the percentage of immature neutrophils in human BM remained unchanged, while mature neutrophils increased in both NDMM and treated MM patients compared to healthy individuals (Fig. 3K, Supplementary Figure S.10A and B).

Conventional DCs (cDCs) show a less activated phenotype in MM-bearing mice

Having demonstrated an increase in the proportion of effector T cells within the lymphoid compartment in MM-bearing mice, we questioned which antigen presenting cells (APCs) within the 5T33MM-TME could potentially induce this T-cell phenotype. Hereto, we performed a differential NicheNet analysis to predict how MM modulates the interactions between the different APCs and (effector) T cells in the spleen, which harbors the highest numbers of T cells. Interestingly, while in naïve mice, neutrophils, monocytes, B cells and cDCs all displayed multiple predicted ligand-receptor interactions with T cells, in MM-bearing mice, the interactions with effector T cells were strongly skewed towards *Ccr7*$^{+}$ activated cDCs (Supplementary Figure S.11A). Hence, cDCs might be important players in the generation of anti-tumor responses in the MM-TME. Remarkably, the role and function of various DC subsets remain poorly investigated in MM. Therefore, we explored our scRNA-seq data to unravel the heterogeneity and activation states of the DC compartment within the MM-TME and healthy tissue. Using the publicly available DC atlas provided by Liu et al. [24], we were able to annotate 16 clusters in the mouse MM DC compartment, including six progenitor clusters and 10 DC (or precursor-DC) clusters (which included precursor plasmacytoid DCs (pre-pDCs)), pDCs and cDCs (Fig. 4A, Supplementary Figure S.11B-C). The cDCs could be further subdivided into *Ccr7*$^{+}$cDCs (also termed migDCs or mregDCs [25]), pre-cDC1s, cDC1s, pre-cDC2s, cDC2s, pro-DC3s and DC3s. Individual clusters were annotated based on the expression of known marker genes (Fig. 4A, Supplementary Figure S.11C).

Within the DC compartment of the 5T33MM model, pDCs seemed to decrease, whereas the pDC_IFN cluster, which expressed additional IFN-associated genes (*Ifit2*, *Ifi211*, *Rsad2*, *Irf7*) and was enriched for gene ontology (GO) terms associated with "response to virus", "innate immune response" and "regulation of type I interferon production", was exclusively present in MM-bearing mice, and was most abundant at 14 DPI (Fig. 4C, Supplementary Figure S.11C–E). This increase in pDCs was also confirmed via flow cytometry at 14 DPI (Fig. 4E).

Among the cDCs, the pre-cDC1s, cDC1s, cDC2as, DC3s, and *Ccr7*$^{+}$cDCs were more prominent in splenic tissue when compared to BM tissue, as the BM mainly included progenitor cells and precursor-cDCs (pre-cDC2 and pro-DC3) (Fig. 4B-D), which aligns with the fact that DCs arise in the BM. Only pDCs fully differentiate in the BM, whereas cDCs leave the BM in a precursor stage and differentiate into cDC subsets in peripheral tissues [26]. Strikingly, MM induced the recruitment of progenitors in the spleen (Fig. 4B), which is consistent with observations in other tumor models [27]. Flow cytometry analysis on the TME of end-stage 5T33MM mice revealed an increase (in BM) of all cDC subsets, which was very pronounced for cDC2s. More specifically, in the spleen, cDC1s decreased at 14 and 20 DPI, cDC2s percentages remained unaltered, and CCR7^{+}cDCs, which contain both cDC1s and cDC2s, significantly increased at end-stage of disease (Fig. 4E-F).

Next, we assessed the functional state of the cDC subsets by flow cytometry and observed a significant increase in cDC-activation (CD80, CD86, CD40) at 7 DPI in most subsets (Fig. 4G, Supplementary Figure S.12A–D). At this critical time point, cancer cells homed and

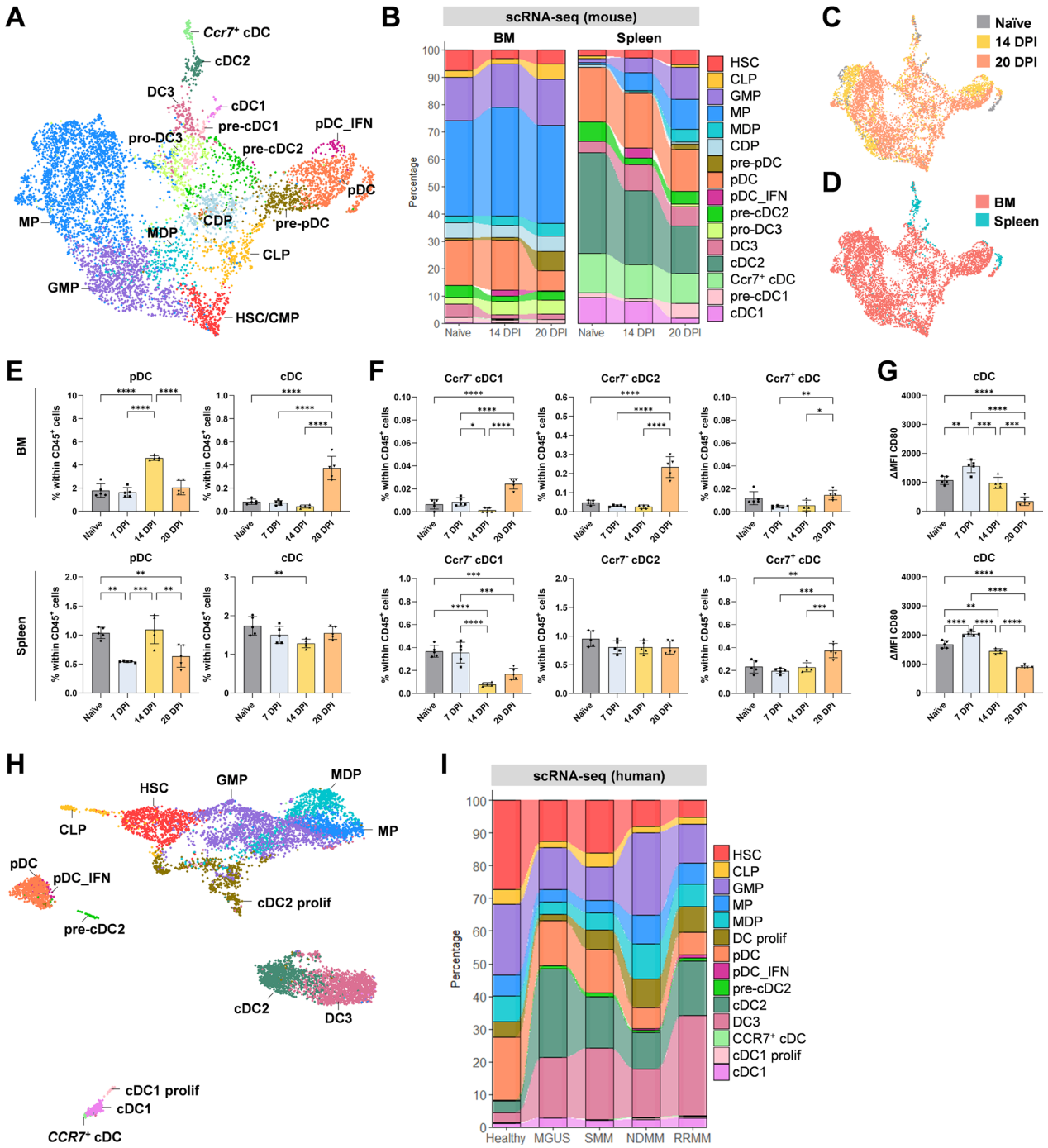

Fig. 4 Conventional DCs (cDCs) show a less activated phenotype in MM-bearing mice. (**A**) UMAP plot shows high-resolution subclustering of the dendritic cell (DC) compartment within the murine scRNA-seq dataset. (**B**) Bar graph shows the frequency of the different DC subsets with the murine BM and spleen across different stages of disease, including naïve mice and 5T33MM mice at 14 DPI and 20 DPI, analyzed using the murine scRNA-seq dataset. (**C-D**) UMAP embedding as shown in panel A but colored according to (C) stage of disease; including naïve mice and 5T33MM mice at 14 DPI and 20 DPI, and (D) tissue of origin; including BM and spleen. (**E–F**) Bar graphs show the frequency of (E) pDCs and cDCs and (F) cDC subsets within the $CD45^+$ cells in murine BM (top) and spleen (bottom) across different stages of disease, analyzed using flow cytometry. n = 5 per group. (**G**) Bar graphs show the ΔMFI (median fluorescence intensity) of CD80 in total cDCs derived from murine BM (top) and spleen (bottom) across different stages of disease, analyzed using flow cytometry. n = 5 per group. (**H**) UMAP plot shows high-resolution subclustering of the DC compartment within the human BM scRNA-seq dataset. (**I**) Bar graph shows the frequency of the different DC subsets within the human BM scRNA-seq dataset across different stages of disease. Error bars represent mean values ± SD. Statistical analysis was performed by Ordinary One-way ANOVA. ns: $p \geq 0.05$, *$p < 0.05$, **$p < 0.01$, ***$p < 0.001$, and ****$p < 0.0001$

began to proliferate in hematopoietic sites (BM and spleen in 5T33MM-bearing mice) suggesting recognition and uptake by cDCs, inducing the activation of the latter. However, at 14 DPI and 20 DPI, the expression of activation markers decreased, indicating a suppressed/less activated phenotype across all cDC subsets upon tumor progression (Fig. 4G, Supplementary Figure S.12A–D). This was also observed, though to a lesser extent, at the transcriptome level (Supplementary Figure S.12E).

When correlating our murine dataset with the patient-derived dataset, based on the expression of canonical genes, we found that the abundance of precursor cells fluctuated between the different stages of disease (Fig. 4H and I, Supplementary Figure S.13A and B). Although mature cDC subsets were in a minority in murine BM, we could observe distinct well represented mature cDC subsets in human BM. In the diseased BM, we observed a massive increase in cDC1, cDC2s and DC3s, with DC3s being the most abundant population in RRMM patients (Fig. 4H-I). *CCR7*$^{+}$cDCs, which can encompass mature cDC1s and cDC2s [25], were absent at precursor and early disease stages, but similarly to the mouse dataset, were found to be increased at NDMM and were also present at RRMM (Fig. 4I, Supplementary Figure S.13B). Very similar to the murine data, the pDC_IFN cluster was exclusively present in the BM of NDMM patients and also increased in RRMM patients. GO terms related to immune activation such as "response to virus", "response to IFNα" and "response to IFNβ", were highlighted in this subset, suggesting the induction of an immune response (Fig. 4H-I, Supplementary Figure S.13C and D).

In conclusion, our data highlights a parallel evolution of the DC heterogeneity within the human and murine MM-TME, with a reduced activation state of the cDCs in later stages of the disease.

Anti-CD40 agonist (αCD40) therapy induces DC activation and T-cell activation ex vivo

To address the reduced activation of cDCs at end-stage of disease, the use of DC-boosting therapies could be a promising solution. CD40 ligation was shown to activate DCs and to be required for cross-priming of CTL-responses by DCs [28, 29]. CD40 is therefore an emerging target for cancer immunotherapy and preclinical results using anti-CD40 (αCD40) agonist antibodies have indeed shown its potential in enhancing DC-activation and promoting sustained anti-tumor immune responses [30], thus offering a potential avenue for improving patients' outcomes in several solid cancers. However, the effect and mechanism of αCD40 agonist therapy in MM remains to be elucidated.

To assess the effect of αCD40 on MM-derived cDCs, we collected BM and spleens from 5T33MM-bearing mice, which were sacrificed at 14 DPI, and incubated total BM and spleen samples for 24 or 72 h with αCD40 therapy (clone FGK4.5) ex vivo (Fig. 5A). αCD40 therapy significantly reduced tumor load in the spleen, as measured by the amount of viable idiotype^{+} plasma cells, and inhibited tumor cell proliferation at 72h (Fig. 5B-C, Supplementary Figure S.14A). To determine which immune compartments contributed to the anti-tumor effects induced by αCD40 therapy in the spleen, we first assessed the number and activation status of cDCs by flow cytometry. We observed a slight increase in the percentage of cDCs, as well as a significant increase in their expression of CD80 and CD86 (Fig. 5D-E). Of note, CCR7^{+}cDCs were activated to a higher extent compared to CCR7^{-}cDCs after 24h and 72h of αCD40 therapy (Supplementary Figure S.14C). Subsequently, αCD40 therapy resulted in higher CD4^{+} and CD8^{+} T-cell proliferation and a significant increase in their potency to produce IFN-γ (Fig. 5F). Intriguingly, NKT cells, but not NK cells, showed a significant increased proliferation, however, both showed increased IFN-γ production upon αCD40 therapy (Fig. 5G). Notably, while the αCD40 resulted in an increased proliferation and activation of T and NK cells, their frequency within the immune population was reduced upon ex vivo αCD40 treatment (Supplementary Figure S.14D). This could be a compensatory response to the increase in other CD40-expressing cells, such as B cells (Supplementary Figure S.14B). Finally, αCD40 therapy had no major effects on frequencies of myeloid cells including neutrophils, eosinophils, Ly6C^{+} monocytes and F4/80^{+} macrophages (Supplementary Figure S.14E).

To corroborate our findings obtained using murine 5T33MM samples, we examined the efficacy of αCD40 therapy (clone G28.5) on freshly isolated primary BM samples from four MM patients (Supplementary Fig. 15A). Upon 48h ex vivo culture with αCD40 therapy, while approximatively 80% of the total BM cells and CD138^{+} plasma were still alive (Supplementary Fig. 15B–D), the anti-tumor effects were rather limited as measured by the amount of PI^{-}CD138^{+} cells (Supplementary Fig. 15E). However, while the proportion of cDCs was not significantly altered and highly variable among patients (Supplementary Figure S.15F-G), we observed a remarkable increase in the expression of CD86 (but not CD80) upon 48h of αCD40 therapy in all analyzed MM patients (Supplementary Fig. 15H). Knowing that CD86 is typically expressed at higher levels during early stages of DC activation, and CD80 in fully matured DCs [31], we hypothesize that the ex vivo culture and experimental setup limited the potential of αCD40 therapy to induce full maturation of DC.

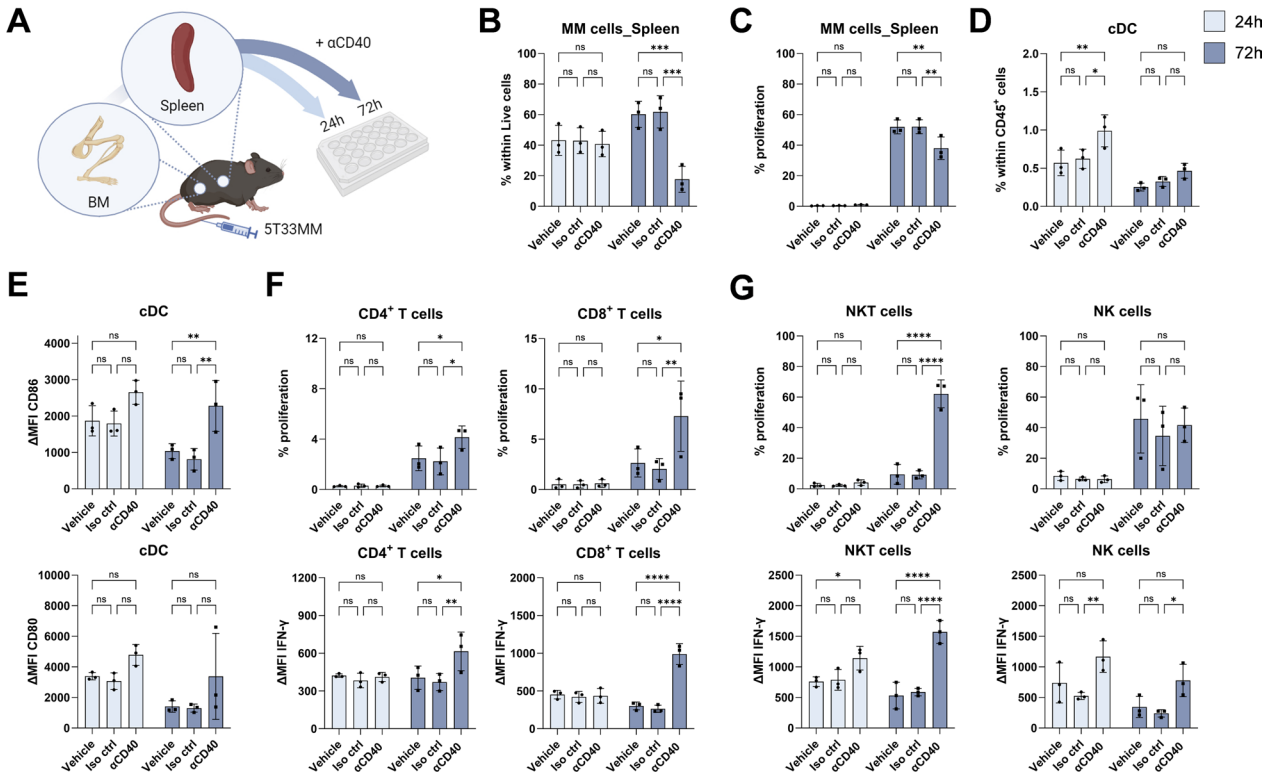

Fig. 5 Anti-CD40 agonist (αCD40) therapy induces DC activation and T-cell activation ex vivo. (**A**) Schematic outline of the experimental procedure. BM and spleen cells from 14 DPI 5T33MM mice were ex vivo treated with 10 µg of αCD40 therapy or isotype control (Iso ctrl) for 24h and 72h. n = 3 per condition. (**B-C**) Bar graphs show the percentage of (B) living MM cells and (C) proliferation of MM cells in spleen after 24h and 72h of αCD40 therapy, analyzed using flow cytometry. (**D-E**) Bar graphs show (D) the percentage of total cDCs within $CD45^+$ cells, and (E) the ΔMFI (median fluorescence intensity) of CD86 and CD80 in total cDCs in spleen after 24h and 72h of αCD40 therapy, analyzed using flow cytometry. (**F-G**) Bar graphs show the percentage of proliferation (top), as well as the ΔMFI (median fluorescence intensity, bottom) of IFN-γ in $CD4^+$ T cells, $CD8^+$ T cells, NKT cells and NK cells in spleen after 24h and 72h of αCD40 therapy, analyzed using flow cytometry. Error bars represent mean values ± SD. Statistical analysis was performed by a two-way ANOVA. ns: $p \geq 0.05$, *$p < 0.05$, **$p < 0.01$, ***$p < 0.001$, and ****$p < 0.0001$

Overall, ex vivo administration of αCD40 therapy resulted in successful activation of cDCs and effector cells, leading to a reduction in tumor load.

αCD40 therapy induces DC activation and T-cell activation, resulting in short-term anti-tumor effects in the 5T33MM model

Since αCD40 therapy showed immune-activating and anti-tumor activity in MM ex vivo, we aimed to further validate these findings in vivo. First, we investigated the impact of a single dose of αCD40 therapy, administered ip at 6 DPI, in 5T33MM-bearing mice (Fig. 6A). αCD40 therapy resulted in a significant reduction in measurable M-protein levels in serum and a decrease in tumor burden in the spleen, whereas only a slight trend could be observed in the BM (Fig. 6B).

Given the potential of αCD40 therapy to reduce 5T33MM tumor-load in vivo, we aimed to elucidate the underlying anti-tumor mechanisms. Therefore, we treated 5T33MM-bearing mice with αCD40 therapy at 6 DPI and analyzed the immune compartment by flow cytometry at 24h (7 DPI), 72h (9 DPI) and one week (14 DPI) after therapy (Fig. 6C). Upon αCD40 therapy, the percentage of cDCs were significantly increased 72h after treatment, mainly caused by an increase in cDC2s (Fig. 6D, Supplementary Figure S.16A). Moreover, pDCs seemed to increase shortly after αCD40 therapy (24h) in the BM, but decreased at later time points after therapy in BM and spleen (Fig. 6E).

Corroborating the ex vivo data, αCD40 therapy significantly increased cDC-activation in cDC1s, cDC2s and $CCR7^+$cDCs in BM and spleen, especially after 24h and 72h, and to some extend this was still visible one week after αCD40 therapy (Fig. 6F, Supplementary Figure S.16B-C). Furthermore, while the percentage of $CD4^+$ T cells and $CD8^+$ T cells was not increased, and the $CD4^+$ T cell-proportion even decreased at 14 DPI upon αCD40 therapy, a significant increase in IFN-γ production could be observed by the latter upon αCD40 therapy (Fig. 6G-I). Moreover, in both BM and spleen,

$CD4^+FoxP3^+$Tregs were significantly decreased after αCD40 therapy (Supplementary Figure S.16D), a phenomenon that has also been demonstrated in other cancer models [30]. In the same line, although NK and NKT cells proportions decreased, their potency to produce IFN-γ was significantly augmented 24h after αCD40 therapy (Fig. 6J-K). These data suggest that NK and NKT cells may be involved in the initial anti-tumor response, whereas, T-cells, especially $CD4^+$ T-cells, were mainly activated at later timepoints after αCD40 therapy, potentially through activated cDCs, in the 5T33MM model. Importantly, this successful immune activation resulted in a significant drop in tumor burden one week after αCD40 therapy (Fig. 6L).

In conclusion, these data provide evidence of the potential of cDC activation by αCD40 therapy which resulted in durable T-cell activation in the 5T33MM model and could hence be used to counteract, at least part of the MM-mediated immune suppression, thereby forming an ideal combination partner for (immuno)therapies.

Discussion

Immunotherapies designed to stimulate the patient's immune response show significant clinical potential [32]. In this respect, understanding the dynamic changes in the immune cell compartment during disease progression and post-treatment could expand the field of immunotherapeutic approaches even more. ScRNA-seq datasets have been previously generated in other immunocompetent MM models, such as the Vκ*MYC model [33]. However, to our knowledge, our study is the first to comprehensively map the immune cell compartment of an immunocompetent MM model (the 5TMM mouse model), while also drawing correlations with human MM at different stages of the disease. Although a main limitation of our animal model is the rapid progression of MM, reaching end-stage of the disease within three weeks, our temporal single-cell transcriptomic analysis revealed strong similarities in the immune cell compartment between murine and human MM, thereby demonstrating the clinical relevance of the 5T33MM model to study MM immunobiology and evaluate (novel) immunotherapeutic approaches.

Based on scRNA-seq and high parameter flow cytometry analysis of the MM-TME, we demonstrated an enrichment in NK cells, NKT cells, T cells, and cDCs already at early stages of MM progression in the murine 5T33MM model, indicating an initial immune response. These findings are in line with previous studies in patients, in which substantial changes within the immune microenvironment were seen as early as the MGUS stage, including an enrichment of NK cells, T cells, and non-classical $CD16^+$ monocytes [7, 10, 34]. In addition, myeloid cells in MGUS patients showed a less activated phenotype, which was accompanied with immunosuppressive properties [35].

Moreover, within the T-cell compartment, we observed a substantial decrease in $CD4^+$ T cells in human MM-BM samples. Recent studies have shown that $CD4^+$ T cells are critical for effective anti-MM responses [19], and showed that their reduction is linked to poor prognosis and decreased treatment efficacy in MM [36]. In mice, we report a shift from naïve-like T-cells towards activated/effector T cells upon MM progression in the 5T33MM model. This shift was associated with a notable decrease in IFN-γ production, along with the display of characteristics suggestive of an exhausted phenotype (e.g. *Tox*, *Havcr2*, *Vsir*, *Lag3*, *Ctla4*, *Pdcd1*). Similar findings were observed in human by de Jong et al., where a decrease in naïve ($CCR7^+$) $CD4^+$ T cells in MM patients was accompanied by an increase in effector $CD8^+$ T cells and IFN-responsive $CD4^+$ and $CD8^+$ T cells (IFIT1/2/3) [37]. In

(See figure on next page.)

Fig. 6 αCD40 therapy induced DC activation and T-cell activation, resulting in short-term anti-tumor effects in the 5T33MM model. (**A**) Schematic outline of the experimental procedure. 5T33MM-inoculated mice received 100 µg of αCD40 therapy or isotype control (Iso ctrl) at 6 DPI. Mice were sacrificed when the control mice reached end-stage of disease. n = 5–6 per group. (**B**) Bar graphs show the tumor load of αCD40 treated 5T33MM mice sacrificed at end-stage of disease. Tumor load was assessed via the M-protein in serum, and by the percentage plasmacytosis in spleen and BM. (**C**) Schematic outline of the experimental procedure. 5T33MM-inoculated mice received 100 µg of Iso ctrl or αCD40 therapy at 6 DPI. Mice were sacrificed at 24h (7 DPI), 72h (9 DPI) and one week (14 DPI) after αCD40 therapy. n = 4 per group. (**D-E**) Bar graphs show the percentage of (D) total cDCs and (E) pDCs within $CD45^+$ cells in BM and spleen, at indicated timepoints in panel C, analyzed using flow cytometry. (**F**) Bar graphs show the ΔMFI (median fluorescence intensity) of CD80 and CD86 in total cDCs from BM (top) and spleen (bottom), at indicated timepoints in panel C, analyzed using flow cytometry. (**G-H**) Bar graphs show (G) the percentage of $CD4^+$ T cells and $CD8^+$ T cells within $CD45^+$ cells, and (H) the ΔMFI (median fluorescence intensity) of IFN-γ in $CD4^+$ T cells and $CD8^+$ T in BM (top) and spleen (bottom), at indicated timepoints in panel C, analyzed using flow cytometry. (**I**) Representative flow cytometry plots show the frequency of IFN-γ in T cells in BM (top) and spleen (bottom) after αCD40 therapy or Iso ctrl, analyzed using flow cytometry. (**J-K**) Bar graphs show (J) the percentage of NK cells and NKT cells, and (K) ΔMFI (median fluorescence intensity) of IFN-γ in NK cells and NKT cells in BM (top) and spleen (bottom), at indicated timepoints in panel C, analyzed using flow cytometry. (**L**) Bar plots show the tumor load of αCD40 treated 5T33MM mice sacrificed at 14 DPI. Tumor load was assessed via the M-protein in serum, and by the percentage plasmacytosis in spleen and BM. Error bars represent mean values ± SD. Statistical analysis was performed by Mann–Whitney U-test (for 2 groups) and two-way ANOVA (for multiple groups). ns: $p \geq 0.05$, *$p < 0.05$, **$p < 0.01$, ***$p < 0.001$, and ****$p < 0.0001$

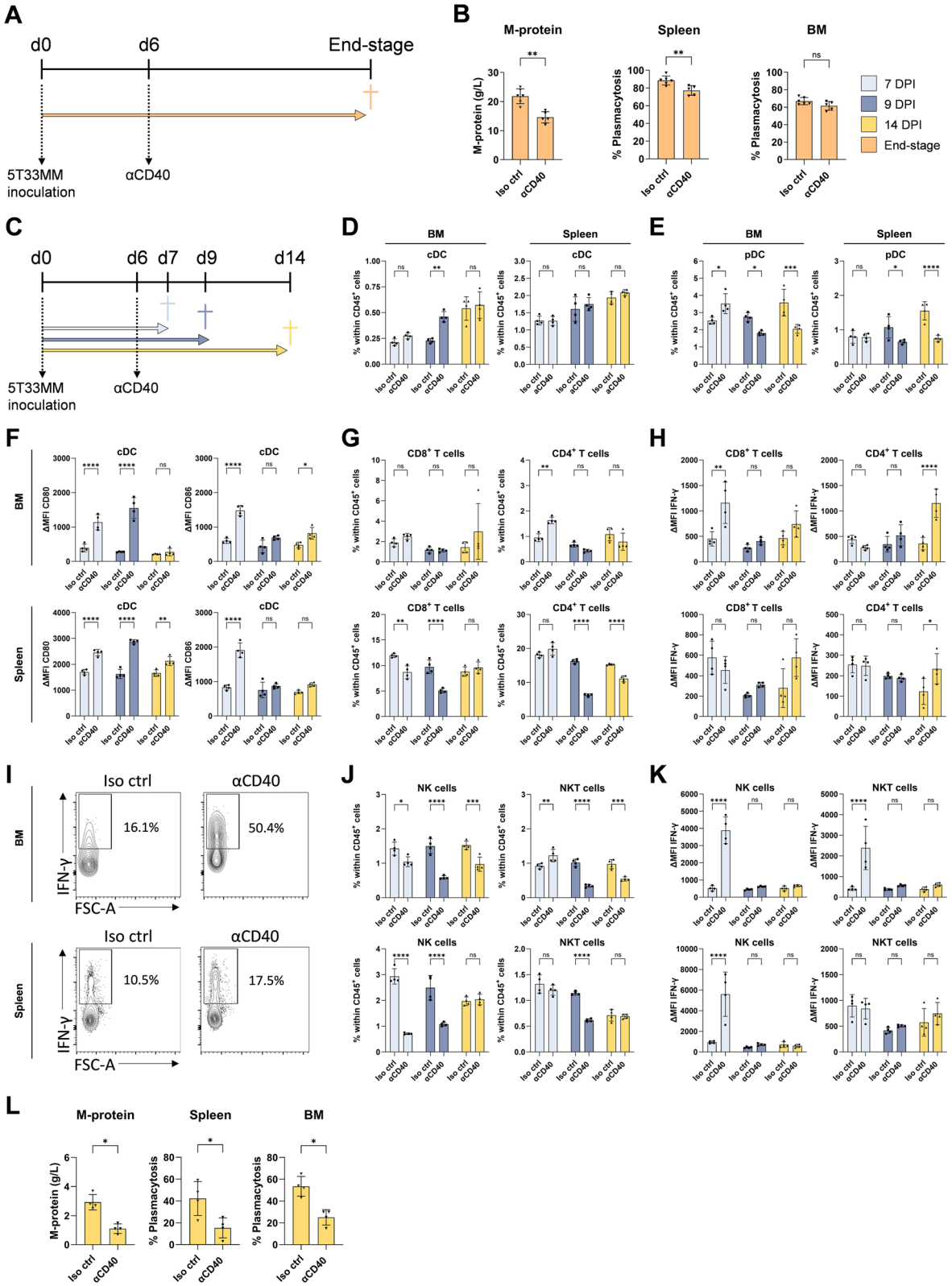

Fig. 6 (See legend on previous page.)

mice engineered to carry MM lesions, a similar progressive rise in activated T cells was reported, with $CD8^+$ T cells displaying a $CD44^+CD62L^-$ effector phenotype and sequentially expression of exhaustion markers such as PD-1, TIGIT, and LAG3 [38]. Additionally, previous studies in MM have linked impaired T-cell function to the upregulated expression of exhaustion markers [10, 34, 39]. As a result, extensive research is being conducted on the use of immune checkpoint inhibitors in combination with immunotherapy for MM [40]. Our dataset could serve as a valuable resource in evaluating how clinically relevant checkpoints evolve with tumor progression.

Besides the emergence of an exhausted T-cell population during MM disease progression, immunosuppressive cell types in the TME are described to impede immunotherapeutic responses. Among these cell types, myeloid-derived suppressor cells (MDSC) have been previously studied by our group using the 5TMM models [14, 22]. Specific targeting of myeloid cells using anti-GR1, targeting MDSCs, or using tasquinimod, a small molecule inhibitor targeting the neutrophil marker S100A9, has been shown to result in increased T-cell activation and reduced tumor burden in the 5TMM model, clearly demonstrating the importance of this cell population in hampering the anti-tumor immune responses [14, 41]. We now demonstrate that neutrophils infiltrating MM exhibit diverse activation states, with less mature neutrophils accumulating in the TME upon tumor-progression. Interestingly, the most mature neutrophils showed a pronounced IFN-signature at 14 DPI, but decreased expression of IFN-associated genes at end-stage of the disease. An enrichment in IFN-inducible genes was previously observed in patient-derived MM cells and microenvironmental cells, including $CD14^+$ monocytes and T cells, during disease progression [42]. In solid tumor models, the expression of IFN-stimulated genes in neutrophils was linked to an anti-tumoral phenotype and increased immunotherapy responses, suggesting that neutrophils at 14 DPI in the 5T33MM model could have a more pronounced anti-tumoral potential, when compared to end-stage of the disease [42]. We demonstrated that depleting neutrophils in the 5T33MM model resulted in a significant drop in tumor load at end-stage of disease, strengthening the notion that neutrophils have immunosuppressive properties in the 5T33MM model [43].

Unlike growth-promoting myeloid cells, the presence of cDCs (e.g. cDC1) is associated with improved outcomes in several cancers such as lung cancer and breast cancer [44, 45]. We observed a significant increase in cDCs, mainly due to cDC2s, in end-stage 5T33MM mice. cDC2s have been reported to be dysfunctional in MM [46]. Accordingly, our data showed a decreased activation of DCs upon disease progression in the 5T33MM model. However, upon administration of αCD40-agonist therapy, we demonstrated an increase in cDCs numbers, especially in cDC2, and an increased activated phenotype in all cDC subsets. Since cDC2s are considered to efficiently activate $CD4^+$ T cells [47], we hypothesize that cDC2s could be responsible for the increased activation of $CD4^+$ T cells upon αCD40 therapy in the 5T33MM model.

In addition, the infiltration of Tregs in the BM is adversely correlated with clinical outcome in MM patients [48]. We demonstrated that upon αCD40-agonist therapy, $CD4^+FoxP3^+$Tregs were significantly decreased in the 5T33MM model. This effect has also been observed in other cancer models [30], though the impact appears to be model-specific [49]. As such, it has been reported that αCD40 therapy converts Tregs into IFN-γ producing Type I $CD4^+$ T effector cells, driven by cDC1 induced IL-12 and IFN-γ signaling [50].

Previous studies demonstrated the potential of inducing antibody-dependent cell-mediated cytotoxicity against CD40-positive MM cells using an anti-CD40 monoclonal antibody (rhuCD40 mAb) [51, 52]. Though CD40 is highly expressed by the B-cell lineage and there has been evidence of CD40 expression on MM cells [53], CD40 expression in 5T33MM cells and human BM $CD138^+$ cells was rather low and varied across patients (data not shown). Moreover, our findings show that ex vivo treatment with αCD40-agonist therapy on human and mouse MM samples, did not significantly affect 5T33MM survival and proliferation (data not shown) and did not increase the tumor load. In addition, we demonstrate the immune activating and subsequent anti-MM responses upon αCD40-agonist therapy in vivo and ex vivo using the 5T33MM model and primary human MM-BM samples.

Currently, phase I/II clinical trials are ongoing, investigating the potential of anti-CD40 agonist therapy in solid cancers, but also in B cell lymphoma [54]. The fact that MM patients are not included in these trials, highlights the need for pre-clinical evidence of the efficacy of αCD40 therapy in MM. Our study provides the first pre-clinical evidence of the immune activating and therapeutic potential of αCD40 therapy in MM. Of note, we believe αCD40 therapy could be of particular interest for patients with minimal residual disease and in combination therapy.

Overall, our findings demonstrate the strong alignment between the immune compartment of the TME of 5T33MM and human MM, as well as the evolution of the immune compartment across different stages of MM in mouse and human. This detailed analysis of the MM-TME could prove beneficial in improving the rationale for therapeutic strategies. The online tool we

provided (www.single-cell.be/Laouimmunology/5T33MMimmunekinetics) allows to easily explore gene expression data for individual genes and signatures, as well as to download lists of differentially expressed genes for all clusters. Therefore, the insights on the specific immune landscapes across the different disease stages provided in this resource could be exploited for the design of future clinical trials on personalized immunotherapy and combination therapies. Although our data has proven the potential of αCD40 therapy, further research will be required to identify the most effective combination therapies with αCD40 therapy for the treatment of MM.

Abbreviations

αCD40	Anti-CD40 agonist
APC	Antigen presenting cells
BCMA	B-cell maturation antigen
BM	Bone marrow
CAR	Chimeric antigen receptor
cDC	Conventional dendritic cell
CLP	Common lymphoid progenitor
DE	Differential expression
DPI	Days post-tumor inoculation
FACS	Fluorescence-activated cell sorting
FCS	Fetal calf serum
GMP	Granulocyte-monocyte progenitors
GO	Gene ontology
GP	Granulocyte precursors
GPRC5D	G protein-coupled receptor class C group 5 member D
HSC	Hematopoietic stem cell
HVG	Highly variable genes
Iv	Intravenously
Ip	Intraperitoneally
MDP	Monocyte-dendritic cell progenitors
MDSC	Myeloid-derived suppressor cell
MGUS	Monoclonal gammopathy of undetermined significance
MM	Multiple myeloma
MP	Monocyte precursors
NDMM	Newly diagnosed multiple myeloma
NKT	Natural killer T cells
PCA	Principal component analysis
pDC	Plasmacytoid dendritic cell
PFS	Progression free survival
Prolif	Proliferation
RBC	Red blood cell lysis
RRMM	Relapsed/refractory multiple myeloma
ScRNA-seq	Single-cell RNA-sequencing
SD	Standard deviation
SE	Standard error
SMM	Smoldering multiple myeloma
TI	Tumor infiltrating
TME	Tumor microenvironment
UMAP	Uniform manifold approximation and projection
UMI	Unique molecular identifier

Supplementary Information

The online version contains supplementary material available at https://doi.org/10.1186/s13045-024-01629-3.

Additional file 1.

Acknowledgements
We thank Charlotte Van De Walle, Carine Seynaeve, and Nadia Abou for their administrative and technical assistance. We are also grateful to the VIB Single Cell Core, VIB Flow Core Ghent, and VIB Nucleomics for their support and access to the instrument park (vib.be/core-facilities). Additionally, we extend our appreciation to the VUB Flow Core for their support and expertise.

Author contributions
E.V., K.D.V. and D.L. designed the experiments. E.V., H.S., N.V., R.F., P.M.R.B, and E.J.C. performed the experiments. E.V. and D.K. performed analyses on the experimental data. E.V. and D.K. performed bioinformatics analyses. A.D.B. provided human samples. Ke.V. generated the online tool. E.V., K.D.V. and D.L. wrote the manuscript. Ka.V. gave advice on the experimental design and manuscript. K.D.V. and D.L. supervised the study.

Funding
E.V was supported by Prijs Kankeronderzoek – Oncologisch Centrum Vrije Universiteit Brussel, Emmanuel van der Schueren grant of Kom op tegen Kanker (KOTK_VUB/2022/13033) and Koning Boudewijnstichting. N.V. is supported by a predoctoral grant from FWO Vlaanderen (FWOSB110). P.M.R.B. is supported by a predoctoral grant from FWO Vlaanderen (1154722N). K.D.V is supported by grants from FWO, Kom op tegen Kanker and Vrije Universiteit Brussel spearhead research programs. D.L. is supported by grants from FWO, Kom op tegen Kanker, Stichting tegen kanker, VIB and Vrije Universiteit Brussel.

Availability of data and materials
The generated scRNA-seq dataset on the 5T33MM-TME described in this article can be accessed via our interactive webserver www.single-cell.be/Laouimmunology/5T33MMimmunekinetics. This tool facilitates the evaluation of gene expression and permits the download of differentially expressed gene lists. Additionally, the mouse scRNA-seq raw data and gene expression matrices are deposited at GEO (NCBI) under accession number GSE271306. Further data supporting the findings of this study can be obtained from the corresponding author upon request.

Declarations

Ethics approval
Mice: All experimental procedures, follow-up and housing complied with the guidelines of the Belgian Council for Laboratory Animal Science and were approved by the Ethical Committee for Animal Experiments of the Vrije Universiteit Brussel (LA1230281, CEP 19-281-3, CEP 20-281-5, CEP 23-281-5, CEP 23-281-6, CEP 23-281-14). Human samples: This study was conducted in compliance with the Declaration of Helsinki and received approval from the University Hospital of Brussels (B.U.N. 143201838414). All patients provided informed consent after the nature and possible consequences of the study had been explained.

Competing interests
The authors declare no competing interests.

Author details
[1]Laboratory of Dendritic Cell Biology and Cancer Immunotherapy, VIB Center for Inflammation Research, Brussels, Belgium. [2]Translational Oncology Research Center, Lab of Hematology and Immunology, Vrije Universiteit Brussel, Laarbeeklaan 103, 1090 Brussels, Belgium. [3]Lab of Cellular and Molecular Immunology, Brussels Center of Immunology, Vrije Universiteit Brussel, Pleinlaan 2, 1050 Brussels, Belgium. [4]VIB Single Cell Core, VIB, Ghent-Louvain, Belgium. [5]Department of Biomedical Molecular Biology, Ghent University, 9052 Ghent, Belgium. [6]Translational Oncology Research Center, Lab of Hematology and Immunology, Universitair Ziekenhuis Brussel (UZ Brussel), Laarbeeklaan 101, 1090 Brussels, Belgium.

Received: 5 July 2024 Accepted: 26 October 2024
Published online: 07 November 2024

References

1. Kumar SK, et al. Multiple myeloma. Nat Rev Dis Primer. 2017;3:1–20.
2. Mohyuddin GR, Chakraborty R, Cliff ERS, Derman BA. Clinician preferences on treatment of smoldering myeloma: a cross-sectional survey. eClinicalMedicine. 2023;65:102272.

3. Rodriguez-Otero P, et al. GPRC5D as a novel target for the treatment of multiple myeloma: a narrative review. Blood Cancer J. 2024;14:1–13.
4. Wang Q, et al. An alternative fully human anti-BCMA CAR-T shows response for relapsed or refractory multiple myeloma with anti-BCMA CAR-T exposures previously. Cancer Gene Ther. 2024;31:420–6.
5. Dang M, et al. Single cell clonotypic and transcriptional evolution of multiple myeloma precursor disease. Cancer Cell. 2023;41:1032-1047.e4.
6. Tirier SM, et al. Subclone-specific microenvironmental impact and drug response in refractory multiple myeloma revealed by single-cell transcriptomics. Nat Commun. 2021;12:6960.
7. Zavidij O, et al. Single-cell RNA sequencing reveals compromised immune microenvironment in precursor stages of multiple myeloma. Nat Cancer. 2020;1:493–506.
8. Schinke C, et al. Characterizing the role of the immune microenvironment in multiple myeloma progression at a single-cell level. Blood Adv. 2022;6:5873.
9. de Jong MME, et al. An IL-1β-driven neutrophil-stromal cell axis fosters a BAFF-rich protumor microenvironment in individuals with multiple myeloma. Nat Immunol. 2024;25:820–33.
10. Pilcher W, et al. Cross center single-cell RNA sequencing study of the immune microenvironment in rapid progressing multiple myeloma. Npj Genomic Med. 2023;8:1–18.
11. Asosingh K, Radl J, Van Riet I, Van Camp B, Vanderkerken K. The 5TMM series: a useful in vivo mouse model of human multiple myeloma. Hematol J Off J Eur Haematol Assoc. 2000;1:351–6.
12. Vanderkerken K, Asosingh K, Croucher P, Van Camp B. Multiple myeloma biology: lessons from the 5TMM models. Immunol Rev. 2003;194:196–206.
13. Vanderkerken K, et al. Organ involvement and phenotypic adhesion profile of 5T2 and 5T33 myeloma cells in the C57BL/KaLwRij mouse. Br J Cancer. 1997;76:451–60.
14. Fan R, et al. Tasquinimod suppresses tumor cell growth and bone resorption by targeting immunosuppressive myeloid cells and inhibiting c-MYC expression in multiple myeloma. J Immunother Cancer. 2023;11:e005319.
15. Lun ATL, McCarthy DJ, Marioni JC. A step-by-step workflow for low-level analysis of single-cell RNA-seq data with Bioconductor. F1000Research. 2016;5:2122.
16. Xie X, et al. Single-cell transcriptome profiling reveals neutrophil heterogeneity in homeostasis and infection. Nat Immunol. 2020;21:1119–33.
17. Salcher S, et al. High-resolution single-cell atlas reveals diversity and plasticity of tissue-resident neutrophils in non-small cell lung cancer. Cancer Cell. 2022;40:1503-1520.e8.
18. Firestone RS, et al. CD8 effector T cells enhance teclistamab response in BCMA-exposed and -naïve multiple myeloma. Blood Adv. 2024;8:1600–11.
19. Zhang X, et al. Characterization of CD4+ T cell-mediated cytotoxicity in patients with multiple myeloma. Cell Immunol. 2018;327:62–7.
20. Andreatta M, et al. Interpretation of T cell states from single-cell transcriptomics data using reference atlases. Nat Commun. 2021;12:2965.
21. Bukhari S, Henick BS, Winchester RJ, Lerrer S, Adam K, Gartshteyn Y, Maniar R, Lin Z, Khodadadi-Jamayran A, Tsirigos A, Salvatore MM, Lagos GG, Reiner SL, Dallos MC, Mathew M, Rizvi NA, Mor A. Single-cell RNA sequencing reveals distinct T cell populations in immune-related adverse events of checkpoint inhibitors. Cell Rep Med. 2023;4(1):868. https://doi.org/10.1016/j.xcrm.2022.100868.
22. Van Valckenborgh E, et al. Multiple myeloma induces the immunosuppressive capacity of distinct myeloid-derived suppressor cell subpopulations in the bone marrow. Leukemia. 2012;26:2424–8.
23. Kiss M, et al. IL1β promotes immune suppression in the tumor microenvironment independent of the inflammasome and gasdermin D. Cancer Immunol Res. 2021;9:309–23.
24. Liu Z, et al. Dendritic cell type 3 arises from Ly6C+ monocyte-dendritic cell progenitors. Immunity. 2023;56:1761-1777.e6.
25. Maier B, et al. A conserved dendritic-cell regulatory program limits antitumour immunity. Nature. 2020;580:257–62.
26. Verheye E, et al. Dendritic cell-based immunotherapy in multiple myeloma: challenges, opportunities, and future directions. Int J Mol Sci. 2022;23:904.
27. Barisas DAG, Choi K. Extramedullary hematopoiesis in cancer. Exp Mol Med. 2024;56:549–58.
28. Bennett SR, et al. Help for cytotoxic-T-cell responses is mediated by CD40 signalling. Nature. 1998;393:478–80.
29. Schoenberger SP, Toes RE, van der Voort EI, Offringa R, Melief CJ. T-cell help for cytotoxic T lymphocytes is mediated by CD40-CD40L interactions. Nature. 1998;393:480–3.
30. Murgaski A, et al. Efficacy of CD40 agonists is mediated by distinct cDC subsets and subverted by suppressive macrophages. Cancer Res. 2022;82:3785–801.
31. Schmidt SV, Nino-Castro AC, Schultze JL. Regulatory dendritic cells: there is more than just immune activation. Front Immunol. 2012;3:274.
32. Xu L, et al. Targeted immunotherapy: harnessing the immune system to battle multiple myeloma. Cell Death Discov. 2024;10:1–17.
33. Croucher DC, et al. Longitudinal single-cell analysis of a myeloma mouse model identifies subclonal molecular programs associated with progression. Nat Commun. 2021;12:6322.
34. Jing W, et al. Combined immune checkpoint protein blockade and low dose whole body irradiation as immunotherapy for myeloma. J Immunother Cancer. 2015;3:2.
35. Bailur JK, et al. Early alterations in stem-like/marrow-resident T cells and innate and myeloid cells in preneoplastic gammopathy. JCI Insight. 2019. https://doi.org/10.1172/jci.insight.127807.
36. Visram A, Dasari S, Anderson E, Kumar S, Kourelis TV. Relapsed multiple myeloma demonstrates distinct patterns of immune microenvironment and malignant cell-mediated immunosuppression. Blood Cancer J. 2021;11:45.
37. de Jong MME, et al. The multiple myeloma microenvironment is defined by an inflammatory stromal cell landscape. Nat Immunol. 2021;22:769–80.
38. Larrayoz M, et al. Preclinical models for prediction of immunotherapy outcomes and immune evasion mechanisms in genetically heterogeneous multiple myeloma. Nat Med. 2023;29:632–45.
39. Zelle-Rieser C, et al. T cells in multiple myeloma display features of exhaustion and senescence at the tumor site. J Hematol Oncol. 2016;9:116.
40. Liu Z, et al. Immune checkpoint inhibitors for multiple myeloma immunotherapy. Exp Hematol Oncol. 2023;12:99.
41. De Veirman K, et al. Multiple myeloma induces Mcl-1 expression and survival of myeloid-derived suppressor cells. Oncotarget. 2015;6:10532–47.
42. Gungabeesoon J, et al. A neutrophil response linked to tumor control in immunotherapy. Cell. 2023;186:1448-1464.e20.
43. Ma H, et al. Interferon-alpha promotes immunosuppression through IFNAR1/STAT1 signalling in head and neck squamous cell carcinoma. Br J Cancer. 2019;120:317–30.
44. Szpor J, et al. Dendritic cells are associated with prognosis and survival in breast cancer. Diagnostics. 2021;11:702.
45. Zilionis R, et al. Single cell transcriptomics of human and mouse lung cancers reveals conserved myeloid populations across individuals and species. Immunity. 2019;50:1317-1334.e10.
46. Jiang J, et al. Distinct mechanisms of dysfunctional antigen-presenting DCs and monocytes by single-cell sequencing in multiple myeloma. Cancer Sci. 2023;114:2750–60.
47. Saito Y, Komori S, Kotani T, Murata Y, Matozaki T. The role of type-2 conventional dendritic cells in the regulation of tumor immunity. Cancers. 2022;14:1976.
48. Alrasheed N, et al. Marrow-infiltrating regulatory T cells correlate with the presence of dysfunctional CD4+PD-1+ cells and inferior survival in patients with newly diagnosed multiple myeloma. Clin Cancer Res Off J Am Assoc Cancer Res. 2020;26:3443–54.
49. Hoves S, et al. Rapid activation of tumor-associated macrophages boosts preexisting tumor immunity. J Exp Med. 2018;215:859–76.
50. Maltez V, et al. Agonistic anti-CD40 converts Tregs into Type 1 effectors within the tumor micro-environment. Preprint at https://doi.org/10.1101/2022.10.17.512537. 2022.
51. Hayashi T, et al. Recombinant humanized anti-CD40 monoclonal antibody triggers autologous antibody-dependent cell-mediated cytotoxicity against multiple myeloma cells. Br J Haematol. 2003;121:592–6.

52. Hussein M, et al. A phase I multidose study of dacetuzumab (SGN-40; humanized anti-CD40 monoclonal antibody) in patients with multiple myeloma. Haematologica. 2010;95:845–8.
53. Qi C, et al. Co-expression of CD40/CD40L on XG1 multiple myeloma cells promotes IL-6 autocrine function. Cancer Invest. 2015;33:6–15.
54. Djureinovic D, Wang M, Kluger HM. Agonistic CD40 antibodies in cancer treatment. Cancers. 2021;13:1302.

Publisher's Note